

JGR Space Physics



RESEARCH ARTICLE

10.1029/2023JA032083

A Novel Backtracing Model to Study the Emission of Energetic Neutral Atoms at Titan

Tyler Tippens¹ , Elias Roussos² , Sven Simon^{1,3} , and Lucas Liuzzo⁴ 

¹School of Earth and Atmospheric Sciences, Georgia Institute of Technology, Atlanta, GA, USA, ²Max Planck Institute for Solar System Research, Göttingen, Germany, ³School of Physics, Georgia Institute of Technology, Atlanta, GA, USA, ⁴Space Sciences Laboratory, University of California, Berkeley, Berkeley, CA, USA

Key Points:

- We describe a new backtracing model to produce synthetic energetic neutral atom (ENA) images at Titan using a realistic, point-like detector
- When magnetic field draping is included, our model reproduces the intensity and morphology of ENA emissions imaged during Cassini's TA flyby
- Qualitative features in ENA images are highly sensitive to the time-varying ambient Saturnian field and the viewing geometry of the detector

Correspondence to:

T. Tippens,
tyler.tippens@eas.gatech.edu

Citation:

Tippens, T., Roussos, E., Simon, S., & Liuzzo, L. (2024). A novel backtracing model to study the emission of energetic neutral atoms at Titan. *Journal of Geophysical Research: Space Physics*, 129, e2023JA032083. <https://doi.org/10.1029/2023JA032083>

Received 14 SEP 2023
Accepted 26 DEC 2023

Abstract To study the emission of energetic neutral atoms (ENAs) at Titan, we have developed a novel model that takes into account a spacecraft detector's limited field of view and traces energetic magnetospheric particles backward in time. ENAs are generated by charge exchange between Titan's atmospheric neutrals and energetic magnetospheric ions. By tracing these ions through the draped electromagnetic fields in Titan's environment, we generate synthetic ENA images and compare them to Cassini observations from the TA flyby. Our model can reproduce the intensity and morphology of the observed images only when field line draping is included. Using a realistic detector geometry is necessary to determine the influence of this draping on the ENA images: the non-uniform fields eliminate a localized feature of increased ENA flux, which is a different effect than in models utilizing an infinitely extended detector. We demonstrate that ENA observations from TA contain signatures of the time-varying Saturnian magnetospheric environment at Titan: the modeled ENA emission morphology and the effect of field line draping are different for the background field vectors measured during the inbound and outbound legs of TA. The visibility and qualitative effect of the draping on observed ENA images vary strongly between different detector locations and pointings. Depending on the viewing geometry, field line draping may add segments of elevated flux to the synthetic ENA images, remove such segments, or have no qualitative effect at all. Our study emphasizes the challenges and the potential for remote sensing of Titan's interaction region using ENA imaging.

1. Introduction

Saturn's largest moon Titan (radius $R_T = 2,575$ km) has a substantial atmosphere, composed of mostly nitrogen (98%) and methane (1%), with its density at the surface being half again larger than at Earth. The moon also possesses an ionosphere generated primarily by solar UV ionization (e.g., Cravens et al., 2010; Coates et al., 2011; Galand et al., 2014, and references therein). Titan orbits Saturn (radius $R_S = 60,268$ km) at a distance of $20.3 R_S$, which, under average solar wind conditions, corresponds to the outer regions of the planet's magnetosphere (Bertucci et al., 2009). During the entirety of the Cassini mission, the spacecraft encountered Titan outside of its parent planet's magnetosphere during only four out of 126 targeted flybys (T32, T42, T85, and T96, see e.g., Bertucci et al., 2007, 2015; Edberg et al., 2013; Feyerabend et al., 2016; Rymer et al., 2009). Sub-corotating magnetospheric plasma constantly overtakes Titan due to the moon's slower orbital velocity (e.g., Kane et al., 2020; Thomsen et al., 2010). The impinging flow is decelerated by mass loading from Titan's ionosphere, causing the planetary magnetic field to pile up on the ramside and drape around the moon, generating Alfvén wings to the north and south (e.g., Ness et al., 1981, 1982; Neubauer et al., 2006). The ambient electromagnetic fields pick up ions (primarily N_2^+ and CH_4^+) from Titan's ionosphere (e.g., Coates et al., 2012). These pick-up ions have large gyroradii (up to $10 R_T$), and so form an asymmetric pick-up tail that extends into the hemisphere where the convective electric field points away from Titan (Bertucci et al., 2007; Simon et al., 2007b, 2015; Wahlund et al., 2005). The ramside magnetic pileup is stretched along the upstream flank of this pick-up tail and is thus also asymmetric (e.g., Chen & Simon, 2020; Simon et al., 2007b).

Cassini's trajectory during its first targeted flyby of Titan (TA) on 26 October 2004 is shown in the Titan Interaction System (TIIS) in Figure 1. In the TIIS, the X axis points in the direction of corotation, the Y axis points toward Saturn, and the Z axis points northward to complete the right-handed coordinate system. The origin of the TIIS coincides with the center of Titan. Cassini passed over Titan's northern hemisphere on the downstream side while moving toward Saturn, reaching its point of closest approach (1,174 km altitude, indicated by the blue cross in Figure 1) at 15:30 UT. The flyby occurred near the ramside of Saturn's magnetosphere at about 10:36 Local

© 2024. The Authors.
This is an open access article under the terms of the [Creative Commons Attribution License](https://creativecommons.org/licenses/by/4.0/), which permits use, distribution and reproduction in any medium, provided the original work is properly cited.

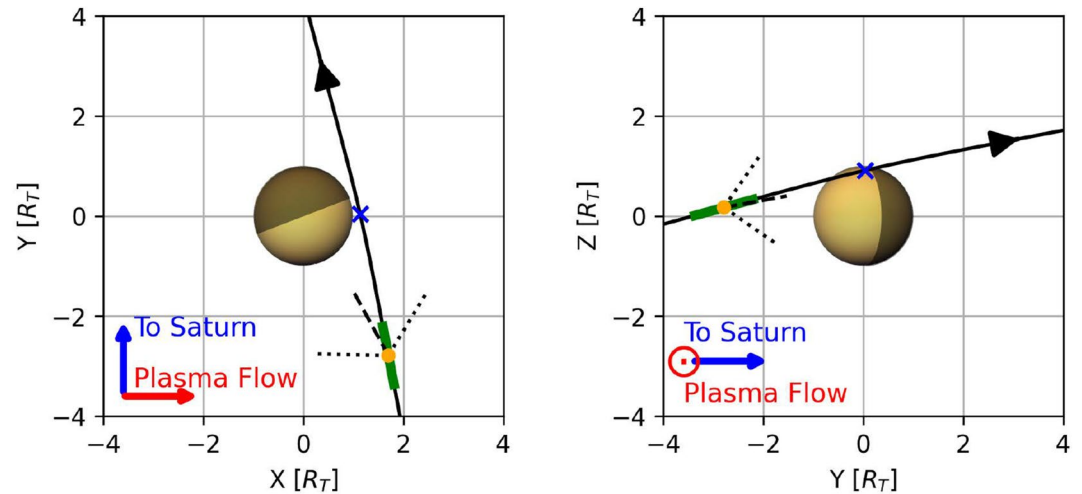


Figure 1. Trajectory of Cassini during the TA flyby of Titan on 26 October 2004, projected onto the $Z = 0$ (left panel) and $X = 0$ (right panel) planes of the TIIS. The shaded portions of the moon were under night at the time of the flyby. The blue cross is the point of Cassini's closest approach to Titan. The green portion of the trajectory indicates the integration time of the observed energetic neutral atom (ENA) image (e.g., Mitchell et al., 2005). The spacecraft's location at the midpoint of this integration interval is indicated by the orange dot, the boresight pointing of the Ion and Neutral Camera (INCA) at this time by the dashed black line, and the limits of the detector field of view in each plane by the dotted black lines to either side.

Time, while Titan was located close to the center of the planet's magnetodisk current sheet (Rymer et al., 2009; Simon et al., 2010b). Measurements taken during TA already indicated that a revision of the more static picture of Titan's magnetospheric environment, derived from data collected by Voyager 1 (e.g., Neubauer et al., 1984), was necessary (Backes et al., 2005; Simon et al., 2010a, 2010b). The ambient magnetospheric field was not directed strictly southward, as often assumed in the pre-Cassini era, but possessed significant components along both the corotation direction and the Saturn-Titan line (see Neubauer et al., 2006, and Section 2.1). The background field vector also changed direction by 33° during the approximately 35 min between Cassini's entry into and exit from Titan's local interaction region (Neubauer et al., 2006). The upstream flow was super-Alfvénic and sub-magnetosonic, with Saturn's magnetospheric ion composition dominated by singly charged oxygen moving with a bulk velocity around 120 km/s relative to Titan (Hartle et al., 2006; Neubauer et al., 2006). The spacecraft observed signatures of Titan's magnetospheric interaction in both magnetic field and plasma parameters (Backes et al., 2005; Neubauer et al., 2006; Wahlund et al., 2005). Cassini passed through the moon's pick-up ion tail in the Saturn-averted hemisphere, sampling Titan's ionospheric ion population (Wahlund et al., 2005), and passed close enough to the moon to detect the upper reaches of the atmosphere (Waite et al., 2005).

A number of modeling studies have investigated Titan's plasma interaction during TA and constrained key features of the moon's induced magnetosphere, including the upstream magnetic pileup region and the magnetic draping pattern. Backes et al. (2005) and Ma et al. (2006) performed magnetohydrodynamic (MHD) simulations and reproduced magnetic field and electron density measurements taken by Cassini along its trajectory, identifying the spacecraft's passage through Titan's northern Alfvén wing and the moon's ionosphere, respectively. Snowden et al. (2007) demonstrated flow shear between light and heavy pick-up ion species from Titan's ionosphere using a multi-fluid model of the moon's environment during TA. Modolo and Chanteur (2008) as well as Lipatov et al. (2014) used hybrid (kinetic ions, fluid electrons) models to characterize major features of the plasma interaction during TA, such as the ramside magnetic pileup, asymmetric pickup tail, and the formation of Alfvén wings. All of these studies utilized different upstream magnetic field vectors, as the high variability in the field over the course of TA prevents the extraction of a unique background field vector that would represent the ambient conditions over extended periods of time (Neubauer et al., 2006).

The magnetic field and particle data analyzed by these models were inherently collected in situ, that is, along the spacecraft's trajectory. Conversely, Cassini's Magnetospheric Imaging Instrument (MIMI, Krimigis et al., 2004) was capable of remotely sensing plasma processes that occur away from the spacecraft's position. MIMI contained a suite of instruments for detecting both charged and neutral energetic particles. In particular, the Ion and Neutral Camera (INCA, Mitchell et al., 1993) returned the first images of energetic neutral atoms (ENAs) originating

from Titan's interaction with its magnetospheric environment (Mitchell et al., 2005). ENAs are generated when energetic ($E \geq 10$ keV) magnetospheric ions (henceforth referred to as “parent ions”) from the ambient Saturnian plasma undergo charge exchange with neutral atoms from Titan's upper atmosphere. Charge exchange interactions neutralize the parent ions (mostly protons, see Mitchell et al., 2005) but do not alter their velocity vectors, with the energy loss to the energetic particles being around 1 eV ($<0.01\%$ of the ions' energies, see Janev & Reiter, 2002; Lindsay & Stebbings, 2005). The newly generated ENAs are decoupled from the electromagnetic fields and continue along straight-line trajectories, as the force of gravity on keV-regime hydrogen atoms is negligible. The INCA instrument, within its 24–55 keV and 55–90 keV sensitivity bands for high-spatial-resolution hydrogen imaging, observed these energetic neutral particles in a way analogous to a camera detecting photons, allowing for remote sensing of the emitted ENAs (e.g., Brandt et al., 2012; Dialynas et al., 2013; Garnier et al., 2008; Mitchell et al., 1993). The resultant ENA images contain an admixture of information on the moon's neutral gas envelope and on the ambient energetic parent ion distribution. In addition, because the ambient ion distribution is strongly modified when these particles travel through the perturbed fields in the vicinity of Titan, the ENA images are strongly affected by the draped electromagnetic field geometry near the moon (e.g., Dandouras & Amsif, 1999; Garnier et al., 2008; Kabanovic et al., 2018; Wulms et al., 2010).

Mitchell et al. (2005) presented the ENA images taken at Titan during the TA flyby and during the subsequent flyby, TB. These images show the observed hydrogen ENA flux into INCA's 24–55 keV energy channel. The incoming ENA flux is recorded in a 32×32 grid (i.e., 32 pixels in each direction) with 3.8° resolution in elevation and 2.8° resolution in azimuth, covering INCA's full 120° by 90° angular field of view (FOV). The integration period of the ENA image from TA (Mitchell et al., 2005) is highlighted in green in Figure 1. The boresight pointing and the INCA field of view at the midpoint of this integration interval are indicated by the dashed and dotted lines, respectively. The ENA image taken during TA reveals a crescent pattern of high ENA flux that wraps around Titan's downstream hemisphere, with an angular segment of low ENA flux observed around the upstream hemisphere. This morphology is qualitatively in line with initial modeling studies of ENA emissions at Titan (Dandouras & Amsif, 1999; Garnier et al., 2008). These studies calculated the detectable ENA flux produced by parent ions which were initialized everywhere around Titan (i.e., even immediately downstream) and moved through uniform electromagnetic fields on circular (gyrating) or drifting trajectories. The authors explained the observed crescent-shaped ENA emission morphology in terms of the energetic parent ions' large gyroradii ($\approx 1\text{--}2 R_T$) and their sense of gyration in a uniform, purely southward ambient magnetic field: for INCA's observation geometry during TA (see Figure 1), ions that have entered the atmosphere gyrate toward the detector on the downstream flank and away from the detector on the upstream flank of Titan (see Figure 1b of Mitchell et al., 2005). Thus, only ENAs generated in Titan's downstream hemisphere could reach the detector during TA. For this reason, ENA observations from TA emphasize the outsized impact of parent ion gyration on the ENA emission signature observable by the INCA detector (see also Garnier et al., 2010).

However, a realistic model of the ENA image taken during TA must include additional aspects of the energetic parent ion dynamics: these particles originate from the uniform plasma upstream of Titan and—before reaching the atmosphere—travel through the draped fields of the moon's induced magnetosphere. These field perturbations were found to drastically alter the trajectories of the energetic parent ions in the vicinity of Titan, including deflecting them around the moon or reversing their field-aligned velocity components (Kabanovic et al., 2018; Regoli et al., 2016; Tippens et al., 2022). Thus, the draped fields ultimately determine where the parent ions can enter Titan's atmosphere and produce ENAs, as well as the velocity vectors of the newly emitted ENAs. Furthermore, INCA detects only a very small fraction of the ENA population emitted from Titan due to the instrument's point-like size compared to the length scales of the plasma interaction, its limited field of view, and the “velocity filtering” of incoming ENA trajectories effected by the collimating charged-particle deflector fins (Krimigis et al., 2004). Many ENAs are emitted away from the detector (see again Figure 1b of Mitchell et al., 2005), and the deflector fins allow only those ENAs which arrive within a particular angle from the boresight vector (described by the instrument's FOV) to reach the detector plate. A realistic model of the ENA emissions detected by Cassini at Titan must therefore take into account the truncation of the emitted ENA population by the instrument geometry.

Brandt et al. (2012) utilized a detector model to analyze ENA observations of Titan's high-altitude hydrogen corona. Their synthetic ENA images were constructed by integrating local ENA production rates in Titan's atmosphere along the detector lines of sight (LOS) to calculate the ENA flux into each pixel. Brandt et al. (2012) compared their modeled ENA images to INCA measurements taken at very high altitudes above Titan ($>20 R_T$)

and found that the moon's dilute hydrogen corona must extend out to about $19 R_T$ altitude to produce the observed ENA emission pattern. The method applied by Brandt et al. (2012) includes a realistic model of the ENA detector itself, in that their model detector observes a highly limited portion of the emitted ENA population with specific velocity vectors (pointing radially toward the detector). However, because these authors focused on ENA emissions from the neutral gas at large distance to Titan, their model did not need to include parent ion deflection by the draped fields within several R_T of the moon. They instead assumed the energetic parent ion distribution to be uniform in space and identical to the distribution measured by Cassini *outside* of Titan's plasma interaction region. Dialynas et al. (2013) studied ENA emissions from Saturn's extended neutral cloud using a similar detector model, again realistically truncating the observable ENA population by considering only ENAs that can reach INCA with velocity vectors inside of the instrument's FOV. These authors modeled Saturn's magnetosphere as a whole rather than the near-Titan environment.

Subsequent models of ENA emissions at Titan by Wulms et al. (2010), Kabanovic et al. (2018), and Tippens et al. (2022) have utilized tracing of the energetic parent ions through the draped fields near the moon in order to determine how the local deflection of the ions maps into the ENA emission morphology. In each of these three studies, the authors launched energetic parent protons from a starting grid in the unperturbed electromagnetic fields outside of Titan's interaction region and traced their trajectories through the draped electromagnetic fields produced by an MHD (Kabanovic et al., 2018; Wulms et al., 2010) or hybrid (Kabanovic et al., 2018; Tippens et al., 2022) model of the moon-plasma interaction. They adopted a statistical approach to model ENA emissions where individual parent ion "macroparticles" represent a large number of real ions with similar positions and velocities. These ion macroparticles are assigned a numerical "weight" (corresponding to the flux of actual ions they represent) which is continuously attenuated as the parent ions move through Titan's atmosphere (which is treated as a continuum) and undergo charge exchange reactions. The weight lost by a parent ion along each segment of its trajectory is carried away by a newly created ENA, which inherits the ion's instantaneous position and velocity and continues along a straight line.

Wulms et al. (2010) and Kabanovic et al. (2018) modeled the ENA emission morphology for INCA's viewing angle during TA. However, these two studies approximated the ENA camera as an infinitely extended plane placed far away from Titan. This plane detector geometry receives ENAs only along specific velocity vectors, namely those within a few degrees of the plane's normal vector. Due to its infinite extent, however, such a detector still captures many more ENAs than an actual, point-like spacecraft instrument would. In particular, ENAs which are generated "behind" Titan from the perspective of a spacecraft (and thus would not be observable) may still be detected by an infinite detector plane since it extends beyond the limb of the moon. Representing the ENA detector in this way was necessary for Wulms et al. (2010) and Kabanovic et al. (2018) due to computational limitations on the number of macroparticles that can be included in a simulation: any given point in the model domain (representing a possible location of a more realistic, point-like ENA detector) does not receive enough ENAs to produce a clear image, even when launching billions of parent ions from the starting grid.

Wulms et al. (2010) traced parent ions through both uniform electromagnetic fields and perturbed fields determined by the MHD model of Backes et al. (2005) for the upstream plasma and field conditions observed during TA. These authors suggested that the crescent of elevated ENA flux is flipped by the field perturbations, from Titan's upstream hemisphere under uniform field conditions to its downstream hemisphere when field draping is included. Thus, the modeled and observed location of the crescent feature only coincide when field draping is considered: the downstream hemisphere is where the crescent resides in the actual TA image (see Mitchell et al., 2005). The results of Wulms et al. (2010) indicate that field line draping plays a critical role in shaping the observable ENA emission morphology. Kabanovic et al. (2018) performed similar tracing of energetic parent ions through the perturbed fields produced by the AIKEF hybrid model (Müller et al., 2011). Unlike the MHD approach of Backes et al. (2005), the hybrid model captures the strong asymmetry in Titan's electromagnetic environment that results from pick-up ion gyration on scales of several R_T . Compared to the MHD model of Backes et al. (2005), Titan's magnetic pileup region in the hybrid model is broader, stretches away from Titan into the Saturn-averted hemisphere, and possesses a weaker peak magnetic enhancement on the ramside. The reduced pileup field strength increases the parent ion gyroradii and thus allows deeper penetration of parent ions into Titan's ramside atmosphere, enhancing the intensity of ENA emissions from this region. The larger extension of the pileup region in the hybrid model, meanwhile, deflects some parent ions away from Titan which are able to emit ENAs in the MHD fields. This effect reduces the intensity of ENA emissions from the moon's wakeside hemisphere. By using a similar, infinitely extended plane detector as Wulms et al. (2010), these authors found

that the draped fields from the hybrid model qualitatively change the ENA emission pattern, compared to the case of uniform fields. However, the effect of field line draping on the ENA emissions is not as strong as was seen by Wulms et al. (2010): the hemispherical reversal in the location of the crescent of high ENA flux between uniform and draped fields is not present in the results from the hybrid model.

Building upon the work of Kabanovic et al. (2018), a subsequent study by Tippens et al. (2022) used the draped fields from the AIKEF hybrid model, but instead utilized a spherical detector located above the atmosphere and concentric with Titan in order to capture the *entirety* of the ENA population that is emitted away from the moon. In order to obtain a comprehensive picture of the physics embedded in the ENA emission morphology, this approach does not include any truncation of observable ENAs by the model detector. Only ENAs which travel toward Titan and are thermalized in the moon's dense lower atmosphere are not detected. Tippens et al. (2022) produced maps of the ENA flux through the detector sphere which show the global ENA emission morphology under various inclinations of the ambient magnetic field against the corotation direction (Simon et al., 2010b). Such different inclinations result from the changing distance between Titan and the center of Saturn's magnetodisk current sheet, caused by, for example, large-scale seasonal warping or more rapid north-south oscillation of the magnetodisk (e.g., Arridge et al., 2008; Simon et al., 2010a, 2010b). Tippens et al. (2022) found that the bulk of the ENAs are emitted into an equatorial "belt" of high ENA flux which encircles the spherical detector along the great circle perpendicular to the ambient magnetospheric field direction. They showed that the field draping partially shields Titan's atmosphere from impinging energetic protons, and so reduces the intensity of ENA emissions by about a third compared to emissions in uniform fields. However, the field draping does *not* qualitatively change the belt-like emission morphology seen by their spherical detector. The results of Tippens et al. (2022) are in contrast to the very strong effect of the draping seen with the plane detector geometry of Wulms et al. (2010), namely the hemispherical reversal of the high flux crescent when field line draping is included. The findings of Tippens et al. (2022), considering the entirety of the ENA population, are also distinct from the weaker yet still qualitative effect of the draping seen by Kabanovic et al. (2018).

The varying conclusions in the literature on the effect of the field draping on the ENA emission morphology emphasize the importance of the chosen model detector geometry on the observable ENA signature. While the effect of the draping is only quantitative when capturing the entirety of the ENA population leaving Titan's atmosphere (Tippens et al., 2022), in reality a spacecraft instrument such as INCA will only ever detect a very small portion of the ENA population, highly filtered in both position and velocity space. The plane detectors used by Wulms et al. (2010) and Kabanovic et al. (2018) approximate this reality by truncating the observable ENA population in velocity space (but not position space). These models suggest a substantial, qualitative contribution of field line draping to the ENA emission pattern observed during TA, but disagree on the strength and morphology of this effect. In order to apply model results to discern the physics seen in actual INCA images from Cassini's Titan flybys, it is necessary to use a model detector which is more true to the instrument geometry and observes only the small corner of phase space that is occupied by the ENA population reaching INCA. However, none of the currently available models have taken into account both a *realistic detector* and included the *field line draping* at Titan.

In this paper, we present for the first time such a realistic ENA detector model in combination with full consideration of the field perturbations from Titan's magnetospheric interaction. Following Kabanovic et al. (2018) and Tippens et al. (2022), our model includes parent ion motion through the draped electromagnetic fields calculated by the AIKEF hybrid model, described in Section 2.1. The detector in our novel ENA model, presented in detail in Section 2.2, is represented using actual instrument locations, pointings, and FOVs. We take into account the "blurring" of signals across adjacent pixels in ENA images described by the detector's point spread function (PSF, see, e.g., Brandt et al., 2012; Dialynas et al., 2013; Mauk et al., 2003), detailed in Section 2.3. We apply this model to analyze the ENA image taken by Cassini during TA. In contrast to any preceding study, our model simultaneously uses both a realistic detector and a parent ion distribution that is locally modified by Titan's perturbed electromagnetic environment.

Our modeled interaction signatures in the thermal plasma along the TA trajectory are validated by comparing the AIKEF output to Cassini electron density measurements (Section 3.1). Our approach generates synthetic ENA images which we compare to the image taken by INCA during TA (Section 3.2). We further apply our synthetic ENA images to assess the influence of field line draping on Titan's observable ENA signature more realistically than has previously been feasible. In Section 3.3 we analyze how three different representations of the detector's

PSF (available in the literature) affect our modeled ENA images. In light of the change in the ambient magnetic field vector over the course of the TA flyby (Neubauer et al., 2006), in that section we also investigate the impact that the choice of the upstream field vector has on the synthetic ENA image. In Section 3.4, we constrain the sensitivity of the modeled ENA image, and in particular any imprint of field line draping, to the instrument's position and pointing. A summary of our findings is provided in Section 4.

2. Model Description

2.1. AIKEF Hybrid Model of Titan's Thermal Plasma Interaction

We use the AIKEF hybrid model (Müller et al., 2011) to determine the three-dimensional structure of the perturbed electromagnetic fields near Titan during the TA flyby. The hybrid model treats the thermal ($E \leq 10$ keV) ions as individual macroparticles and electrons as a massless, charge-neutralizing fluid. Resolving individual ion dynamics is necessary at Titan due to the large gyroradii (up to $10 R_T$; see, e.g., Simon et al., 2007b) of the ionospheric pick-up ions. Furthermore, the hybrid model resolves flow shear between the thermal magnetospheric ions and the ionospheric pick-up species. AIKEF has been used extensively in preceding studies of Titan's magnetospheric interaction and achieved excellent quantitative agreement with Cassini plasma and magnetic field data from several flybys (Feyerabend et al., 2015, 2016; Kabanovic et al., 2018; Müller et al., 2010; Simon & Motschmann, 2009; Simon, Motschmann, & Glassmeier, 2008; Simon, Motschmann, Kleindienst, et al., 2008; Simon et al., 2006, 2007a, 2007b, 2007c, 2009; Tippens et al., 2022). In addition, the model provided the draped electromagnetic fields for preceding studies on ENA emissions at Titan (Kabanovic et al., 2018; Tippens et al., 2022). For this reason, we provide only a brief overview of the input parameters used to model Titan's induced magnetosphere during the TA flyby. For further details on the AIKEF model, the reader is referred to any of our preceding publications.

AIKEF runs on a hierarchical Cartesian grid using the TIS coordinate system $\{X, Y, Z\}$. The simulation domain is a cube which is centered at Titan and extends $\pm 10 R_T$ in each direction. Such a box is large enough for the fields at the edges of the domain to return to their uniform upstream values (see, e.g., Simon & Motschmann, 2009; Regoli et al., 2016). We use three levels of resolution for the grid: $0.208 R_T$ for $|X|, |Y|, |Z| > 4 R_T$, $0.104 R_T$ for $4 R_T \geq |X|, |Y|, |Z| > 2 R_T$ and $0.052 R_T$ for $2 R_T \geq |X|, |Y|, |Z|$. For reference, the thermal O^+ ion gyroradii in the upstream flow are approximately $1.6 R_T$ (see Table 1). The parameters of the impinging thermal flow are initially set to their upstream values everywhere in the domain (see Table 1). Only the thermal plasma population is modeled in AIKEF; the dynamics of energetic ions ($E \geq 10$ keV), which ultimately produce ENAs, are not included in AIKEF due to the numerical infeasibility of solving both high- and low-energy particle dynamics simultaneously (e.g., Tippens et al., 2022). Furthermore, these particles do not contribute appreciably to the currents and field perturbations near Titan (see discussion in Tippens et al. (2022), and references therein).

Due to the observed variation in the ambient magnetospheric conditions at Titan over the course of the TA flyby (e.g., Backes et al., 2005; Neubauer et al., 2006), there is no consensus in the literature on a unique set of uniform and steady-state upstream plasma parameters that could be used in our model. Measurements of the magnetic field as well as the ambient magnetospheric ion and electron energy distributions indicate that Titan was primarily located within Saturn's magnetodisk current sheet during the flyby (Garnier et al., 2010; Németh et al., 2011; Rymer et al., 2009; Simon et al., 2010b). In this regime, the ambient magnetospheric field is oriented mostly southward, but with superimposed fluctuations in the amplitude of the radial field component (i.e., along the $\pm Y$ axis) on time scales of several minutes (Simon et al., 2010b). The orientation of the ambient field vector changed by 33° between Cassini's entry into Titan's induced magnetosphere and its exit from the interaction region around 35 min later (Backes et al., 2005; Neubauer et al., 2006). Furthermore, the ambient electron number density varied significantly in the hours preceding Cassini's entry into and following its exit from Titan's induced magnetosphere during TA (Ma et al., 2006). Thus, it is not feasible to describe the ambient magnetospheric conditions during TA using a single set of parameters.

The absence of a unique set of upstream conditions for modeling Titan's plasma interaction during TA is manifested in the literature: the modeling studies of Backes et al. (2005), Ma et al. (2006), Snowden et al. (2007), and Modolo and Chantaur (2008) all utilized different background magnetospheric field vectors (which vary between studies by up to 19° in orientation and a factor of 1.6 in magnitude) and upstream plasma mass densities (which vary between different studies by up to a factor of 2.6). Furthermore, Ma et al. (2006) used a bulk velocity vector that is inclined 22° away from the X axis, as suggested by Voyager 1 observations (Arridge et al., 2011a, 2011b),

Table 1
Thermal Upstream Plasma Parameters During TA, in TIS Coordinates, Used for the AIKEF Model

Upstream plasma parameter	Case 1 (Outbound magnetic field)	Case 2 (Inbound magnetic field)
Magnetic field (\vec{B}_0)	(1.727, 2.994, -3.584) nT	(0.828, 1.019, -5.697) nT
Field magnitude ($ \vec{B}_0 $)	4.98 nT	5.85 nT
Bulk plasma velocity (\vec{u}_0)	(120, 0, 0) km/s	(120, 0, 0) km/s
Ion number density (n_0)	0.14 cm ⁻³	0.14 cm ⁻³
Ion mass density (ρ_0)	2.24 amu/cm ³	2.24 amu/cm ³
Ion temperature ($kT_{i,0}$)	1,500 eV	1,500 eV
Electron temperature ($kT_{e,0}$)	200 eV	200 eV
Alfvén velocity magnitude ($v_{A,0}$)	72.6 km/s	85.2 km/s
Alfvénic Mach number (M_A)	1.65	1.41
Plasma beta (β)	3.41	2.47
Sound speed (c_s)	134 km/s	134 km/s
Sonic Mach number (M_S)	0.89	0.89
Magnetosound speed (c_{MS})	160 km/s	167 km/s
Magnetosonic Mach number (M_{MS})	0.75	0.72
Local time	10.6	10.6
Subsolar latitude	-23.2°	-23.2°
Subsolar longitude	159°	159°

whereas the other modeling studies assumed the upstream flow to be aligned with the corotation direction (+X). Despite these differences in their selection of upstream parameters, however, all of the aforementioned studies succeeded in reproducing different aspects of the perturbations observed in the electron density (Ma et al., 2006; Modolo & Chanteur, 2008) or magnetic field (Backes et al., 2005; Snowden et al., 2007). Hence, there is some ambiguity regarding the set of (uniform) upstream plasma parameters which would be best suited for our modeling study of Titan's plasma interaction during the TA flyby.

We select a background magnetic field vector of $\vec{B}_{0,1} = (1.727, 2.994, -3.585)$ nT (labeled “Case 1” in Table 1) as the “baseline” for modeling Titan's plasma interaction during TA. We also consider a second model setup that uses a background field of $\vec{B}_{0,2} = (0.828, 1.019, -5.697)$ nT (labeled “Case 2” in Table 1) to constrain the sensitivity of the modeled ENA images to changes in the ambient magnetospheric field. The vectors $\vec{B}_{0,1}$ and $\vec{B}_{0,2}$ are taken from Neubauer et al. (2006), and were calculated by averaging Cassini magnetometer measurements over a period of 80 s just after and a period of 3 min just before Cassini traveled through Titan's interaction region, respectively. The upstream bulk velocity in our model is set to $\vec{u}_0 = (120, 0, 0)$ km/s for both cases, which was used by Neubauer et al. (2006), Snowden et al. (2007), and Modolo and Chanteur (2008). This choice is consistent with observations made by the Cassini Plasma Spectrometer (CAPS) during TA (Szego et al., 2005). This upstream velocity is also well within the range observed during numerous additional Cassini crossings of Titan's orbit (see, e.g., Arridge et al., 2011a, 2011b; Kane et al., 2020; Thomsen et al., 2010).

Within Saturn's magnetodisk current sheet, singly ionized atomic oxygen (O⁺) has double the number density of both H⁺ and H₂⁺ (Bagenal & Delamere, 2011). The contribution of oxygen to the mass density is thus a factor of 32 greater than that of atomic hydrogen and a factor of 16 greater than that of molecular hydrogen. As shown by, for example, Simon et al. (2007b), the thermal hydrogen ions do not make appreciable contributions to the electromagnetic field perturbations near Titan. Since Titan was located within the magnetodisk current sheet during TA (e.g., Simon et al., 2010b), we therefore consider O⁺ as the only thermal ion species in AIKEF (analogous to Snowden et al. (2007), Wulms et al. (2010), Kabanovic et al. (2018), and Tippens et al. (2022)). We use an upstream plasma number density of $n_0 = 0.14$ cm⁻³ for both model cases, similar to values measured by Voyager 1 and Cassini at Titan's orbit in Saturn's magnetodisk current sheet (Arridge et al., 2011a, 2011b; Bagenal & Delamere, 2011; Neubauer et al., 1984). The resulting mass density of 2.24 amu·cm⁻³ is within the

range of values utilized by preceding modeling studies of TA (Backes et al., 2005; Ma et al., 2006; Modolo & Chanteur, 2008; Snowden et al., 2007) and also close to the value of $2.9 \text{ amu}\cdot\text{cm}^{-3}$ measured during the Voyager 1 encounter (Arridge et al., 2011a, 2011b). The observed magnetospheric O^+ temperature near Titan's orbit ranges from below 1,000 eV up to 2,900 eV (e.g., Arridge et al., 2011a, 2011b; Bagenal & Delamere, 2011; Neubauer et al., 1984). We use a temperature of $kT_{i,0} = 1,500 \text{ eV}$ for both cases 1 and 2 as an intermediate value within this range. We set the magnetospheric electron temperature to $kT_{e,0} = 200 \text{ eV}$ in both cases, consistent with Voyager 1 measurements (Neubauer et al., 1984) and within the range of Cassini measurements near Titan when located within Saturn's magnetodisk current sheet (Arridge et al., 2011a, 2011b; Rymer et al., 2009). These values for the temperature and density of the thermal ions, as well as the temperature of the thermal electrons, were also used by Kabanovic et al. (2018) and Tippens et al. (2022), thereby facilitating comparisons to their model results for ENA emissions. Using this combination of parameters, the upstream plasma in our model has an Alfvénic Mach number of $M_A = 1.65$ in case 1 and $M_A = 1.41$ in case 2, and a magnetosonic Mach number of $M_{MS} = 0.75$ in case 1 and $M_{MS} = 0.72$ in case 2. A comprehensive overview of all upstream parameters used is provided in Table 1.

To represent Titan's atmosphere, we include the same neutral profile as was used by Tippens et al. (2022). This profile is consistent with Cassini Ion Neutral Mass Spectrometer (INMS) observations of the moon's atmospheric density during 29 flybys (Cui et al., 2009; Müller-Wodarg et al., 2014; Westlake et al., 2011). Following more recent revision of the INMS sensitivity model, Tippens et al. (2022) multiplied these observed density values by a factor of 2.2 (Teolis et al., 2015). The model atmosphere is spherically symmetric and consists of three species: N_2 , CH_4 , and H_2 . The radial profile of the number density $n_k(h)$ of each species k is given by a barometric law,

$$n_k(h) = n_{0,k} \exp\left(-\frac{h}{H_k}\right), \quad (1)$$

where h is the altitude above Titan's surface, $n_{0,k}$ is the number density of the respective species at the surface, and H_k is the scale height. For nitrogen, we use a surface number density and scale height, respectively, of $n_{0,\text{N}_2} = 4 \cdot 10^{16} \text{ cm}^{-3}$ and $H_{\text{N}_2} = 72.3 \text{ km}$. For methane, the parameters are $n_{0,\text{CH}_4} = 2 \cdot 10^{13} \text{ cm}^{-3}$ and $H_{\text{CH}_4} = 96.6 \text{ km}$. We use different sets of parameters for hydrogen above and below an altitude of 1,225 km: $n_{0,\text{H}_2} = 8.52 \cdot 10^7 \text{ cm}^{-3}$ and $H_{\text{H}_2} = 297.6 \text{ km}$ above, and $n_{0,\text{H}_2} = 5.82 \cdot 10^{13} \text{ cm}^{-3}$ and $H_{\text{H}_2} = 69.8 \text{ km}$ below. This piecewise approach better captures Titan's high-altitude H_2 corona, compared to a single set of parameters for all altitudes (Modolo & Chanteur, 2008). A more detailed discussion of the atmospheric profile used in AIKEF can be found in Tippens et al. (2022).

Titan's ionosphere is generated within AIKEF by a wavelength-dependent photoionization model (EUVAC, Richards et al., 1994) and ion-neutral charge exchange interactions. In the photoionization model, Titan's subsolar point is located at -23.2° latitude and 159.0° west longitude. This configuration corresponds to the orientation of the moon's dayside hemisphere at the time of the TA flyby (Backes et al., 2005). The ion production rate of ion-neutral charge exchange is calculated self-consistently using the neutral density profiles of H_2 , N_2 , and CH_4 , along with the local number density of the magnetospheric O^+ ions (see Feyerabend et al., 2015, 2016, for details).

2.2. A Realistic ENA Detector Model

To overcome the computational challenges associated with the infeasibly large number of parent ions required to generate a clear ENA image (Kabanovic et al., 2018; Wulms et al., 2010), we have developed a novel method utilizing *backtracing* of energetic parent protons, that is, solving their equations of motions with a *negative* time step Δt . We use this method to produce synthetic ENA images using a detector geometry which closely mimics that of INCA. Like Brandt et al. (2012) and Dialynas et al. (2013), we integrate the ENA flux emitted by charge exchange between energetic parent protons and Titan's atmosphere along lines of sight extended out from each surface element (pixel) of the model detector. Our backtracing model builds upon the approaches used by, for example, Liuzzo et al. (2019), Poppe et al. (2018), and Addison et al. (2022) to calculate energetic ion fluxes onto the surfaces of Jupiter's Galilean moons, or by Fatemi et al. (2012) for the terrestrial moon. However, these preceding models do not include charge exchange interactions between backtraced energetic ions and the neutral gas, that is, they assume Liouville's theorem to be applicable everywhere. We trace the energetic protons through the draped electromagnetic fields produced by AIKEF to calculate the detectable ENA flux they emit as they undergo charge exchange with Titan's atmosphere.

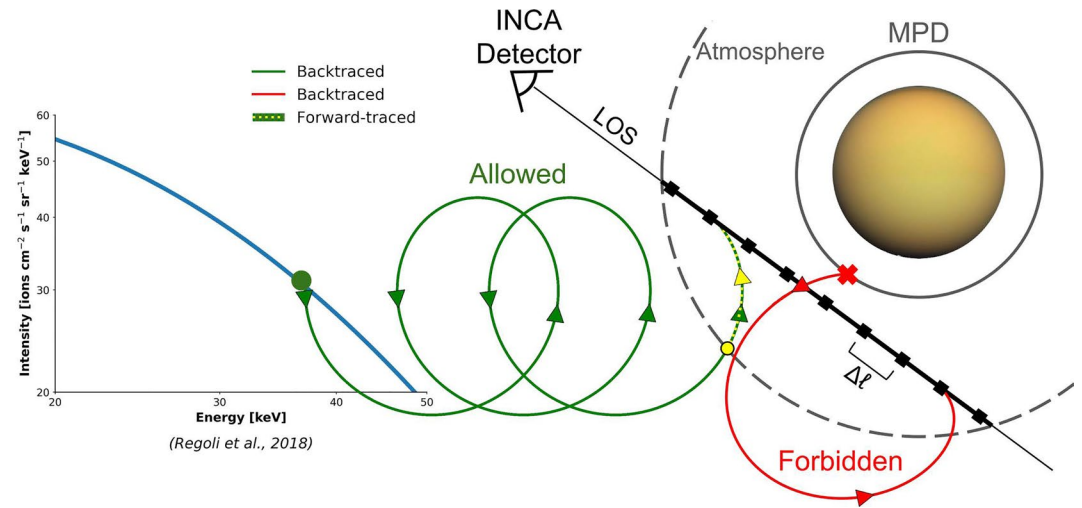


Figure 2. Illustration of the novel ENA backtracing model. The outer boundary of Titan's atmosphere and the minimum passing distance (MPD) are indicated by the dashed and solid gray circles, respectively. The black open angle represents INCA's viewing direction, with the thin black line representing one of the detector's lines of sight at this orientation. Where this line of sight (LOS) passes through Titan's atmosphere it appears in bold, and the discretization of this portion into segments of length $\Delta\ell$ is represented by the black squares. Energetic parent ions are launched from each of these segments and traced backward in time. The backtraced ion trajectory colored red passes below the MPD and so is "forbidden," that is, this parent ion cannot emit ENA flux into the detector. An "allowed" parent ion trajectory is shown in green; this ion is able to reach the ambient plasma outside of Titan's interaction region. It is assigned a numerical "weight" by sampling the ambient energetic proton distribution (indicated by the blue curve) at the energy the ion possesses when it exits the interaction region. The portion of this "allowed" trajectory that passes through the atmosphere is overlaid with the yellow dashed line. We calculate the ENA flux that this parent ion emits toward the ENA detector at its launch point on the LOS. For this purpose, the attenuation Equation 6 for the ion's numerical weight is solved (forward in time) along the trajectory segment within Titan's atmosphere (yellow). The red, green, and yellow arrows along the two trajectories denote the instantaneous velocity vectors of the parent ions. These vectors are *the same* in both the forward-tracing and backtracing pictures.

The simulation domain of the ENA model is the same as that of AIKEF: its center coincides with the center of Titan and it extends $\pm 10R_T$ along each axis of the TIIS. The point-like ENA detector in our model has the same, limited FOV as the INCA detector (90° of azimuth and 120° of elevation) and can be freely positioned and oriented within the simulation domain. To generate a synthetic ENA image for the TA flyby, the model detector is placed along Cassini's trajectory at position $\vec{x} = (1.66, -2.54, 0.24) R_T$, indicated by the orange dot in Figure 1. The model detector's pointing matches that of INCA in the middle of the integration period (green bar in Figure 1) of the actual ENA image from TA. The INCA detector's boresight and FOV in this configuration are indicated by the black dashed and dotted lines in Figure 1, respectively. The boresight unit vector is $\vec{u}_{BS} = (-0.52, 0.85, 0.12)$ and points away from the instrument.

It is sufficient to generate a single synthetic ENA image from the middle of the data integration period (green segment in Figure 1). During image integration, INCA collected ENA counts for all momentary orientations of the detector. Taking into account the time-varying detector orientation, the instrument "cut out" the final image product from this pool of ENA counts to yield the observed ENA emissions for the average pointing of the detector over the course of the integration (Krimigis et al., 2004). Detected ENAs which are not within the detector FOV defined in this way are truncated by the instrument. Thus, the images produced by INCA already account for spacecraft motion and integration time and can be considered a snapshot of the observable ENA flux in the middle of the integration period. Therefore, we can compare them to synthetic ENA images generated using the detector location and pointing at the center of the integration interval (e.g., Krimigis et al., 2004).

A schematic illustration of the ENA model is shown in Figure 2. The model detector's FOV covers part of a sphere, is centered at the boresight, and is discretized with an angular resolution of 0.3° in both azimuth and elevation. This discretization yields a grid of 120,000 unit vectors, each one normal to a specific detector element. The model detector's lines of sight extend from each grid element radially outward along these vectors. One such line of sight is shown in Figure 2 as the straight black line labeled "LOS." Each LOS is associated with a pixel in the synthetic ENA image: only those ENAs which are emitted exactly toward a pixel along its specific LOS can

contribute to the flux into that surface element of the detector. Consequently, the total ENA flux into a certain pixel is the sum of the ENA fluxes emitted by parent ions (covering a range of energies) whose velocity vectors are tangential to its LOS (and also point toward the detector) at different locations within the atmosphere. No ENA flux is generated along any lines of sight which do not intersect Titan's atmosphere at all, and the ENA intensity measured by their associated pixels on the detector is set to zero.

For each LOS, the portions which do intersect the atmosphere are discretized into segments of constant length $\Delta\ell = 0.015 R_T$, shown in Figure 2 separated by bold black squares (not to scale). The resolution $\Delta\ell$ is half of the smallest scale height included in our atmospheric model (see Section 2.1). This ensures that the influence of the non-uniform neutral density on the ENA emissions is resolved by the model. The length ℓ of the portion of a given LOS that intersects Titan's atmosphere ($\ell = N\Delta\ell$, with N the number of segments within Titan's atmosphere) varies between different lines of sight based on the model detector's position and pointing. A parent proton of a given energy E is launched at the center of each segment $\Delta\ell$ and is traced through the draped electromagnetic fields with a *negative* time step $\Delta t < 0$. These fields are obtained at a certain point in time after AIKEF has reached a stationary state. While INCA cannot discriminate between ENAs detected within its 24–55 keV data channel, a 55 keV proton has a gyroradius ($R_g = 2.3 - 2.6R_T$, using the values of $|\vec{B}_0|$ from Table 1) about 1.5 times larger than that of a 25 keV proton ($R_g = 1.5 - 1.8R_T$). The differences in these particles' dynamics, and thus in their ability to emit ENAs, must be taken into account. From each segment $\Delta\ell$, we therefore launch parent ions at seven discrete energies, ranging from 25 to 55 keV in constant increments of 5 keV, to cover the 24–55 keV energy channel in which INCA recorded the ENA image from TA. Each proton is given an initial velocity $v_0 = \sqrt{2E/m}$ (where m is the proton's mass and E its energy) that is directed *anti-parallel* to the respective LOS (pointing toward the detector). It is thus assigned the same velocity vector that an ENA of energy E emitted along the LOS would have at that location. The backtraced protons' trajectories are calculated from Newton's second law of motion and the Lorentz force for a charged particle in electric and magnetic fields (\vec{E} and \vec{B} , respectively):

$$\frac{d\vec{x}}{dt} = \vec{v} \quad \text{and} \quad (2)$$

$$\frac{d\vec{v}}{dt} = \frac{e}{m} (\vec{E} + \vec{v} \times \vec{B}), \quad (3)$$

where \vec{x} is the proton's position, \vec{v} is its velocity, and e is its charge. During each time step, the electric and magnetic field vectors at the proton's position are determined by trilinear interpolation from the field vectors at the nearest eight grid points of the AIKEF field cube. Equations 2 and 3 are solved numerically using the Runge-Kutta method of 4th order accuracy (RK4) and a negative time step $\Delta t < 0$. The size of the time step $|\Delta t|$ is adaptive and is set to 1% of the parent ion's gyroperiod in the *local* magnetic field.

Each parent ion's trajectory is traced backwards in time until it is found to be either “forbidden” or “allowed.” A trajectory is considered *forbidden* if, at any point in time, it passes below the minimum passing distance (MPD, solid gray circle in Figure 2) located at 1,045 km altitude (Garnier et al., 2008; Kabanovic et al., 2018; Tippens et al., 2022; Wulms et al., 2010). The MPD is the altitude below which Titan's atmospheric neutral density is high enough that an emitted ENA will leave the moon's atmosphere with too little energy to be detectable by INCA's 24–55 keV channel (Garnier et al., 2008; Wulms et al., 2010). This depletion occurs due to numerous consecutive charge exchange interactions siphoning energy from the particle as it moves through the dense neutral gas below the MPD (for a detailed discussion see, e.g., Garnier et al., 2008; Tippens et al., 2022; Kabanovic et al., 2018; Wulms et al., 2010). The sample parent ion trajectory shown in red in Figure 2 is forbidden: after launching from a point along a LOS and being traced backward in time, the particle gyrates below the MPD (red cross). This type of trajectory is non-physical when viewed in the forward-tracing picture ($\Delta t > 0$): an energetic parent ion originating from the ambient plasma and taking this path would be required to travel through the dense lower atmosphere or even the solid body of Titan in order to reach the original “launch point” on the LOS. Thus, at a given energy E the LOS segment $\Delta\ell$ is inaccessible to energetic protons from the ambient plasma in the forward-tracing picture. A parent proton with a forbidden trajectory therefore does not contribute ENA flux into the detector pixel associated with this LOS, that is, the flux value assigned to such a particle is set to zero.

A backtraced parent ion trajectory is considered *allowed* if the particle reaches the outer boundary of the AIKEF simulation domain, where the fields have returned to their uniform background values, without ever passing

below the MPD. The trajectory colored green in Figure 2 represents such an allowed parent ion. A 55 keV proton (the highest energy at which we initialize backtraced parent ions) has a gyroradius of about $2.3\text{--}2.6 R_T$ (again using the values of $|\vec{B}_0|$ from Table 1), so it cannot return to Titan from the edge of the AIKEF simulation domain (located $10 R_T$ from the moon) through gyration alone. For an ion with an *allowed* trajectory, the flux it represents can be obtained from the velocity distribution observed outside of the interaction region. To determine whether a parent proton's trajectory is allowed or forbidden, we trace its trajectory backward in time through the field cube from AIKEF but do *not* (yet) consider any interactions between the ion and the neutral gas. In other words, in this initial backtracing step we only determine which parent ions are able to contribute ENA flux to the synthetic ENA image, that is, which ions are able to travel from the LOS into the ambient plasma. ENA generation will be modeled in a subsequent step.

A backtraced energetic proton which reaches the unperturbed electromagnetic fields outside of Titan's interaction region may travel along Saturn's magnetospheric field lines, undergo magnetic mirroring at high latitudes, and return to the moon. Such a returning proton could still become forbidden, if it returns from its bounce close to Titan and travels below the MPD during its second visit to the moon's local interaction region. Regoli et al. (2016) estimated that a bouncing 50 keV proton would be displaced toward downstream (i.e., toward upstream in the backtracing picture) by about $6.7 R_T$. This suggests that a bouncing energetic proton (which may possess a gyroradius of up to $2.6 R_T$) may indeed return to Titan's interaction region. To determine whether the trajectory of such a bouncing proton is allowed or forbidden, it would need to be traced along its bounce path through Saturn's magnetosphere over lengths on the order of $100 R_S$. However, there is currently no model available in the peer-reviewed literature that describes the global shape of the Saturnian magnetospheric field lines threading Titan's orbit at the time of the TA flyby. Therefore, it is not feasible to calculate where the bouncing ions would reenter the AIKEF simulation domain (with accuracies well below $1 R_T$ needed) after traversing these paths. For a more detailed discussion of this issue, we refer the reader to Tippens et al. (2022). In the present study, we proceed analogous to Tippens et al. (2022) and consider any energetic parent ion which reaches the edge of the AIKEF simulation domain to have an allowed trajectory. This approach constitutes an uncertainty in our model that may be addressed in future work by coupling our local interaction model to a global model of Saturn's magnetosphere. Such an approach has already been implemented for energetic ion dynamics at Europa and Callisto, where global magnetospheric models are available (e.g., Addison et al., 2023; Liuzzo et al., 2022).

Parent ions with allowed trajectories are assigned a numerical "weight" $I_0(E_0)$ that represents the intensity of the energetic proton flux at the energy E_0 of the backtraced ion when it reaches the undisturbed plasma outside of Titan's interaction region. Due to acceleration of the ion by the electromagnetic fields, this energy E_0 may be different from the energy E at which the backtraced particle was initially launched from the LOS. The intensity distribution $I(\tilde{E}_0)$, where \tilde{E}_0 is the energy E_0 in units of keV, of the ambient energetic proton flux at Titan's orbit (blue curve on the left of Figure 2) has been determined by Regoli et al. (2018) using Cassini data from all close Titan flybys as well as orbital crossings that occurred far from the moon. This distribution has the form

$$I(\tilde{E}_0) = C \tilde{E}_0 \left[\frac{\tilde{E}_0 + kT(1 + \kappa)}{1 \text{ keV}} \right]^{-(1+\kappa)}, \quad (4)$$

where, to model the ambient energetic proton distribution during TA, we use parameters for magnetospheric current sheet conditions: $\kappa = 4.78$, $C = 2.15 \cdot 10^{12} \text{ 1/(cm}^2 \text{ s sr keV}^2)$, and $kT = 9.31 \text{ keV}$ (Regoli et al., 2018). The pitch angle distribution of energetic protons outside of Titan's interaction region is quasi-isotropic in the energy range of $27\text{--}56 \text{ keV}$, covering nearly all of INCA's $24\text{--}55 \text{ keV}$ channel, so we treat it as isotropic at all seven initial proton energies considered (Garnier et al., 2010). This assumption is consistent with the approaches of Wulms et al. (2010), Kabanovic et al. (2018), and Tippens et al. (2022). The weight assigned to each proton in the ambient plasma is a differential particle flux given by $I_0 = I(\tilde{E}_0)$.

Once a backtraced parent ion with an allowed trajectory has been assigned its weight $I_0(E_0)$, we must determine how much ENA flux it emits into the detector at its initial launch point on the LOS. For this purpose, we return to the point along the ion's backtraced trajectory where it last exited Titan's atmosphere before reaching the unperturbed ambient plasma (illustrated by the yellow dot in Figure 2). Since the ion may gain or lose energy as it moves through the perturbed fields close to Titan, its weight must be adjusted from the value $I_0(E_0)$ in the ambient plasma to the value I_1 at the top of the moon's atmosphere. This adjustment makes use of Liouville's theorem, stipulating the conservation of the distribution function in the absence of ion-neutral interactions and

wave-particle scattering (see, e.g., Kollmann et al., 2019). Liouville's theorem represents a suitable approximation here because the portion of the ion's trajectory between the top of Titan's atmosphere (yellow dot in Figure 2) and the ambient plasma is free of collisions. Furthermore, ion cyclotron waves (which could scatter the protons) have been observed at Titan during only two flybys (namely, T63 and T98, see Russell et al., 2016). These waves were observed only within a segment of length 0.4–0.8 R_T along Cassini's trajectory, or less than 10% of the extension of Titan's interaction region. Due to the highly sporadic occurrence of these waves and the scarcity of available observations, taking into account their effect on the applicability of Liouville's theorem is neither feasible nor necessary.

The adjusted weight I_1 at the top of the atmosphere is determined by the parent ion's weight $I_0(E_0)$ outside the interaction region, its energy in the ambient plasma E_0 , and its energy at the top of the atmosphere E_1 , according to

$$I_1 = \frac{E_1}{E_0} I_0, \quad (5)$$

see Equation 3 of Kollmann et al. (2019). An analogous weight adjustment is made whenever the parent ion exits Titan's atmosphere and, at some point in time, reenters it. However, this adjustment is valid only in the absence of ion-neutral interactions. Therefore, we must use a different method to calculate the progressive loss of weight (and associated ENA generation) that the parent ion experiences due to charge exchange as it moves (in forward time, $\Delta t > 0$) through Titan's atmosphere.

With the backtraced parent protons' weights I_1 at the top of the atmosphere determined, we can find the ENA flux that each one emits into the detector along the LOS from which it was launched. The ENA flux that a parent ion emits at its launch point along the selected LOS is the *only* quantity that is required to compute its contribution to the associated pixel of the synthetic ENA image. Once we have determined the ENA flux that each parent ion emits into the detector, we sum these contributions along each LOS and across all seven discrete energies representing INCA's 24–55 keV channel to form a synthetic ENA image. The energy loss an energetic proton experiences due to a single charge exchange interaction is on the order of only 1 eV, compared to parent ion energies of tens of keV (Janev & Reiter, 2002; Lindsay & Stebbings, 2005). Therefore, as long as an energetic parent ion does not pass through the dense neutral gas below the MPD (and become forbidden), we can calculate the ENA flux that it emits into the detector along a given LOS *after* finding its backtraced trajectory through the atmosphere.

Charge exchange between energetic protons and Titan's atmosphere, leading to ENA generation, is described in our model by attenuation of the parent ion's numerical weight (in forward-time) along its trajectory through the neutral gas. The same approach was used in the models of Wulms et al. (2010), Kabanovic et al. (2018), and Tippens et al. (2022). Charge exchange and ENA generation take place along the yellow dashed portion of the trajectory in Figure 2, where this sample ion passes through the atmosphere. Titan's atmosphere in our ENA model is treated as a continuum that consists of N_2 and CH_4 , with number densities given by the same barometric profiles as in AIKEF (see Equation 1). The energy-dependent cross sections for charge exchange between these two neutral species and energetic protons are shown in Figure 3; the cross sections for nitrogen (colored blue) are from Lindsay and Stebbings (2005) and those for methane (colored red) are from Janev and Reiter (2002). Because the number densities of atmospheric N_2 and CH_4 decay exponentially with altitude, ENA emissions generated near the exobase (around 1,450 km altitude, e.g., Regoli et al., 2016) are at least an order of magnitude more intense than those produced at higher altitudes (Brandt et al., 2012; Tippens et al., 2022; Wulms et al., 2010). Therefore, in our ENA emission model Titan's atmosphere has an outer boundary at $2 R_T$ altitude, which is more than 50 atmospheric scale heights (see Section 2.1). Atmospheric hydrogen is included in AIKEF, but not in the ENA generation model: its number density near Titan's exobase is several orders of magnitude lower than those of nitrogen and methane. Furthermore, the cross section for charge exchange between energetic protons and hydrogen is about two-thirds that of nitrogen and one-third that of methane (Janev & Reiter, 2002; Lindsay & Stebbings, 2005). These factors lead to 1–2 orders of magnitude lower ENA emission intensity from the H_2 component of Titan's atmosphere, compared to N_2 and CH_4 (Amsif et al., 1997).

As an energetic parent ion is backtraced along an allowed trajectory through the atmosphere after launch from a segment of the LOS, we store the path length ds traversed during each time step $\Delta t < 0$ as well as the altitude-dependent atmospheric number densities $n_k = n_k(h)$ and energy-dependent cross sections $\sigma_k = \sigma_k(E)$ of each atmospheric species ($k = N_2, CH_4$, see Figure 3) at its position. In a subsequent step, we calculate (in the forward-tracing picture) the attenuation of the parent proton's numerical weight along the portion of its trajectory

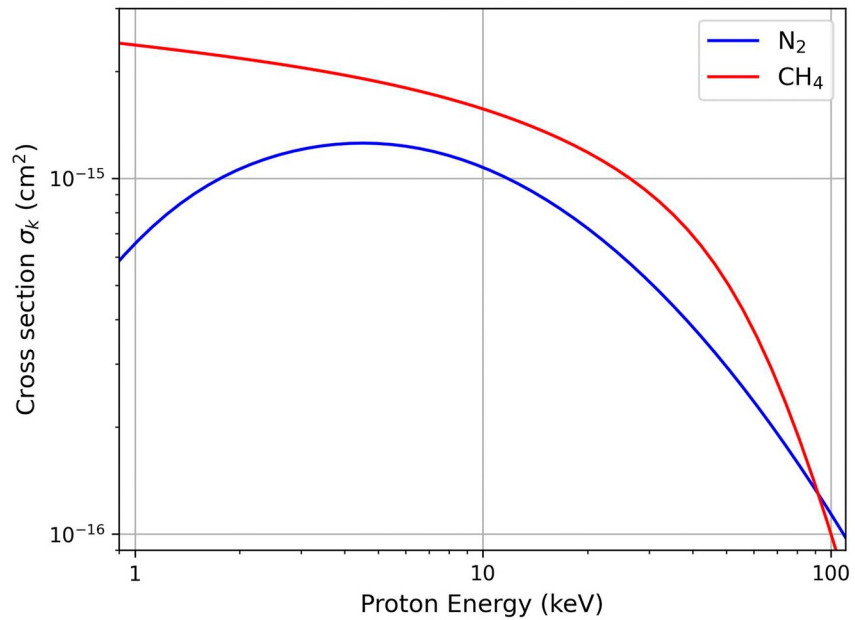


Figure 3. Energy-dependent cross sections for charge exchange reactions of molecular nitrogen (colored blue) and methane (colored red) with energetic protons (Janev & Reiter, 2002; Lindsay & Stebbings, 2005).

within the atmosphere in order to determine the ENA flux it emits into the detector at its original launch point on the LOS. Starting from the parent ion's adjusted weight I_1 at the top of the atmosphere (yellow circle in Figure 2) and now moving forward in time, the ion loses weight dI along a path element ds as

$$dI = -I \left(\sum_k \sigma_k n_k \right) ds, \quad (6)$$

see also Tippens et al. (2022). Equation 6 is integrated forward in time along the parent proton's previously calculated trajectory through the neutral gas, from the top of the atmosphere to its initial “launch point” at the detector LOS, using the RK4 method. We emphasize that there is a difference between the kinetic energy of an energetic proton macroparticle and its numerical weight I . The macroparticle's kinetic energy does *not* change appreciably during charge exchange reactions, and this change is therefore not included in our model (see discussion earlier in this section). Only the weight of the macroparticle is reduced during charge exchange, indicating that a certain number of the actual protons it represents has been converted into ENA flux.

The portion of each detector LOS that lies within Titan's atmosphere is divided into N equally spaced segments $\Delta\ell$, which we label with the index $i = 1, 2, \dots, N$. In general, since the value of $\Delta\ell = 0.015R_T$ is fixed, the number of segments N is different for each of the 120,000 lines of sight we consider. At each segment $\Delta\ell$, we consider $\nu = 7$ launch energies $E_j = 25 \text{ keV} + j \cdot 5 \text{ keV}$, where $j = 0, 1, \dots, \nu - 1$, to find the total ENA flux detected in INCA's 24–55 keV energy channel. The ENA macroparticle that a parent proton of energy E_j generates at its launch point in segment i of the LOS (i.e., at the point where the yellow dashed line merges with the bolded black LOS in Figure 2) carries a flux $|dI_{i,j}|$ along the LOS and into the model detector. The total ENA flux Y_{E_j} at this energy E_j into a certain pixel of the detector is calculated by summing the emissions of parent ions with *allowed* trajectories from all segments $i = 1, 2, \dots, N$ along the pixel's associated LOS (i.e., from each of the segments bounded by the black squares in Figure 2). Because we are free to choose the size $\Delta\ell$ of the segments into which we decompose the portion of the LOS within Titan's atmosphere, we must normalize the contribution of each segment. Hence, the ENA flux Y_{E_j} into the respective detector pixel, carried by ENAs at energy E_j , is given by

$$Y_{E_j} = \frac{1}{N} \sum_{i=1}^N |dI_{i,j}|. \quad (7)$$

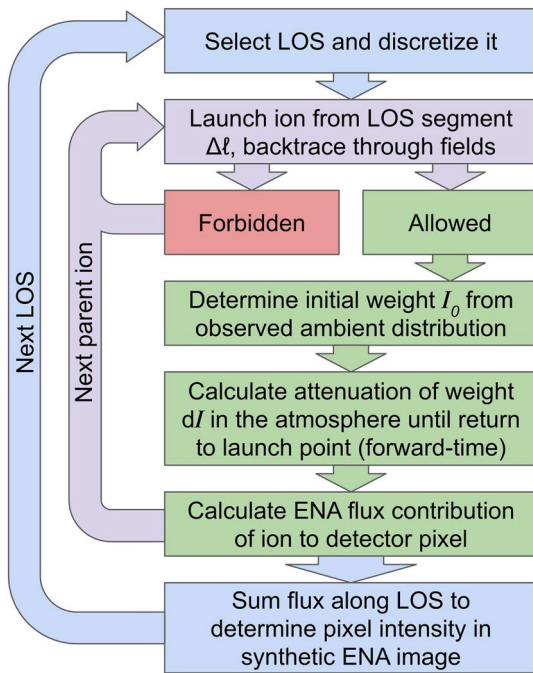


Figure 4. Flowchart summarizing the interplay between the different parts of the ENA detector model.

The sum takes into account each of the N segments $\Delta\ell$ within the atmosphere. For segments of the LOS associated with *forbidden* proton trajectories, the contribution dI_{ij} in the sum of Equation 7 is set to zero. Since $\ell = N\Delta\ell$, each ENA's contribution to the flux Y_{E_j} is weighted by the fraction $\Delta\ell$ of the LOS length ℓ within the atmosphere. This weighting ensures that the ENA flux emitted along a certain LOS into the detector is not artificially increased by merely launching more parent ions along ℓ (i.e., by increasing the number N of segments) or decreased by launching fewer.

The total ENA flux Y into a certain pixel of the model detector does not only take into account contributions from different LOS segments $\Delta\ell$, but also from particles with different energies E_j . The number ν of discrete energies we investigate is set to $\nu = 7$, but constitutes a free parameter in our model. Since the total ENA flux Y into each pixel of the model detector needs to be independent of the number ν of discrete energies considered, another weighting factor is included in this calculation:

$$Y = \frac{1}{\nu} \sum_{j=0}^{\nu-1} Y_{E_j} = \frac{1}{N \cdot \nu} \sum_{j=0}^{\nu-1} \sum_{i=1}^N |dI_{i,j}|. \quad (8)$$

Again, we set $dI_{ij} = 0$ for LOS segments and energies that correspond to forbidden proton trajectories in the backtracing model. The two sums in Equation 8 now include the ENAs generated by all backtraced parent ions with allowed trajectories (i.e., all segments along the LOS and all ENA energies) launched along the pixel's associated LOS. The flowchart in Figure 4 summarizes the process of generating a synthetic ENA image in our model.

Even when remaining above the MPD at all times, the ENAs observed by INCA may have undergone multiple re-ionizations and subsequent neutralizations before reaching the detector (Garnier et al., 2008). However, we consider only the first neutralization of energetic protons into ENAs. Constraining the impact of multiple charge exchange interactions on the observable ENA emissions at Titan (under realistic electromagnetic field conditions) is beyond the scope of the present study. We emphasize that the ENA emission models of Wulms et al. (2010) and Kabanovic et al. (2018) both succeeded in explaining key features of the observed ENA emission pattern from TA by considering only the initial neutralization of impinging energetic protons.

2.3. Post-Processing of Synthetic ENA Images

In order to permit a meaningful comparison between our modeled ENA images and INCA observations, two image processing steps must be performed after the synthetic ENA images have been generated with the method from Section 2.2. The first step is down-scaling of the modeled images to the resolution of the actual INCA detector. The lines of sight of the actual detector have non-zero width in velocity space, that is, each pixel can receive ENAs within a small range of velocity vectors approximating a cone (Krimigis et al., 2004). However, the pixels of the model detector can receive ENAs only along a single direction, defined by the respective LOS. To accommodate this effect, we produce synthetic ENA images with a higher resolution than the images taken by INCA: with an angular resolution of 0.3° in both elevation and azimuth, the model detector produces ENA images that are 400×300 pixels in size. Cassini's INCA detector recorded 24–55 keV hydrogen ENA images with a size of only 32×32 pixels, or with a resolution of about 2.81° in azimuth and 3.75° in elevation. In other words, multiple smaller pixels of our model detector (each of them corresponding to a single, *one-dimensional* LOS) “fill in” the *cone-shaped* LOS associated with a larger pixel of the INCA detector. We therefore rescale the synthetic ENA images to match the resolution of actual images taken by INCA. For this purpose, we apply the `INTER_AREA` interpolation method of the open source image processing library OpenCV (<https://opencv.org/>): the flux value assigned to each pixel in the coarser image is calculated as the average of the flux values from the small pixels on the finer image, located in the same area. When calculating this average, the flux value from each of the smaller pixels is weighted by the relative contribution of its area to the area of the larger pixel. This procedure preserves the mean ENA intensity (averaged over all pixels) of the image after down-scaling, such that

Table 2
Standard Deviation Values in the Literature for the INCA Point Spread Function $\mathcal{P}(r, s)$ in Each Dimension of the Detector, as Defined by Equation 9

Source	λ_r (elevation)	λ_s (azimuth)
Krimigis et al. (2004)	0.91	1.21
Brandt et al. (2012)	1.13	1.51
Dialynas et al. (2013)	1.02	1.66

Note. Subscript r represents elevation and subscript s represents azimuth. The values in the table are taken from Krimigis et al. (2004), Brandt et al. (2012), and Dialynas et al. (2013). However, instead of the standard deviations λ_r and λ_s , these authors give the *full width at half maximum* (F_r and F_s) of the point spread function, that is the width of the distribution in each direction at half its peak value. This quantity has been converted to the standard deviation using the relation $F_{r,s} = 2\sqrt{2 \ln 2} \lambda_{r,s}$. In the studies of Krimigis et al. (2004), Brandt et al. (2012), and Dialynas et al. (2013), the values of $F_{r,s}$ are given in degrees, so we have also divided them by the detector's angular resolution in each direction to match the dimensionless form used in Equation 9. The angular resolution in elevation (subscript r) is $120^\circ/32 = 3.75^\circ$ and in azimuth (subscript s) is $90^\circ/32 = 2.81^\circ$.

reducing the resolution of the synthetic ENA image only slightly blurs the emission features seen by the model detector.

Once the synthetic ENA images have been scaled down to the actual INCA resolution, the second processing step is to convolve them with a point spread function (PSF). The PSF describes INCA's response to a point source of ENAs, which, in an ideal case, would populate only a *single* pixel of the detector with ENA flux. However, in reality ENAs from such a point source are slightly scattered by the foil at the entrance to the detector (Krimigis et al., 2004). This effect is distinct from the non-zero width of each pixel's LOS which we account for by down-scaling: in the ideal case, ENAs from a point source anywhere within a pixel's LOS "cone" would populate only that pixel. Because of the foil scattering, however, some of the resulting ENA signal "bleeds" into pixels surrounding the one whose LOS precisely connects the detector to the point source. The point spread function \mathcal{P} describes this effect quantitatively (e.g., Mauk et al., 2003). The functional form of \mathcal{P} is a normal distribution in each angular direction of the detector:

$$\mathcal{P}(r, s) = \frac{1}{2\pi\lambda_r\lambda_s} \exp\left[-\frac{1}{2}\left(\frac{r-r_0}{\lambda_r}\right)^2\right] \exp\left[-\frac{1}{2}\left(\frac{s-s_0}{\lambda_s}\right)^2\right]. \quad (9)$$

Starting at the center ($r = 0, s = 0$) of the detector, we use the integer variables $r = -15, -14, \dots, 0, \dots, 15, 16$ and $s = -15, -14, \dots, 0, \dots, 15, 16$ to

label each pixel on the detector in elevation and azimuth, respectively. In Equation 9, r_0 and s_0 are the indices of the pixel whose LOS precisely connects to the (hypothetical) point source. The dimensionless parameters λ_r and λ_s are the standard deviations of the PSF in elevation and azimuth, respectively. The "bleedover" $I(r, s)$ from pixel (r_0, s_0) into its neighbors is calculated for each pixel with indices (r, s) according to

$$I(r, s) = \tilde{I}(r_0, s_0)\mathcal{P}(r, s). \quad (10)$$

In this expression, $\tilde{I}(r_0, s_0)$ is the differential ENA flux that travels toward the detector along the LOS connecting the point source to pixel (r_0, s_0) . However, the flux $\tilde{I}(r_0, s_0)$ does *not* represent the value actually detected at pixel (r_0, s_0) : scattering of the incoming ENAs takes place before this flux reaches the detector pixel. Indeed, Equation 10 reveals that the flux detected at pixel (r_0, s_0) is *smaller* than $\tilde{I}(r_0, s_0)$:

$$I(r_0, s_0) = \frac{\tilde{I}(r_0, s_0)}{2\pi\lambda_r\lambda_s} < \tilde{I}(r_0, s_0), \quad (11)$$

since the factor $2\pi\lambda_r\lambda_s$ is greater than unity (see also discussion below and Table 2).

Smearing out our synthetic, down-scaled ENA images with the PSF does *not* introduce or eliminate ENA flux from the image, but only redistributes it across the image. To demonstrate this, we again consider detector pixel (r_0, s_0) in the (down-scaled) synthetic ENA image toward which an ENA flux $\tilde{I}(r_0, s_0)$ is emitted by a point-like source. The flux directed at pixel (r_0, s_0) is spread into surrounding pixels (r, s) by the PSF according to Equation 10. We integrate over the full detector to calculate the total differential flux I associated with ENAs impinging along the LOS of pixel (r_0, s_0) :

$$I = \sum_r \sum_s I(r, s)\Delta s\Delta r \quad (12)$$

$$= \sum_r \sum_s \tilde{I}(r_0, s_0)\mathcal{P}(r, s)\Delta s\Delta r \quad (13)$$

$$\approx \tilde{I}(r_0, s_0) \int_{-\infty}^{\infty} \int_{-\infty}^{\infty} \mathcal{P}(r, s) ds dr. \quad (14)$$

The increments $\Delta r = 1$ and $\Delta s = 1$ are the "size" of the pixels in each direction, here merely indicating an increment of 1 between the indices of neighboring pixels. The approximation of the sums as integrals is valid because

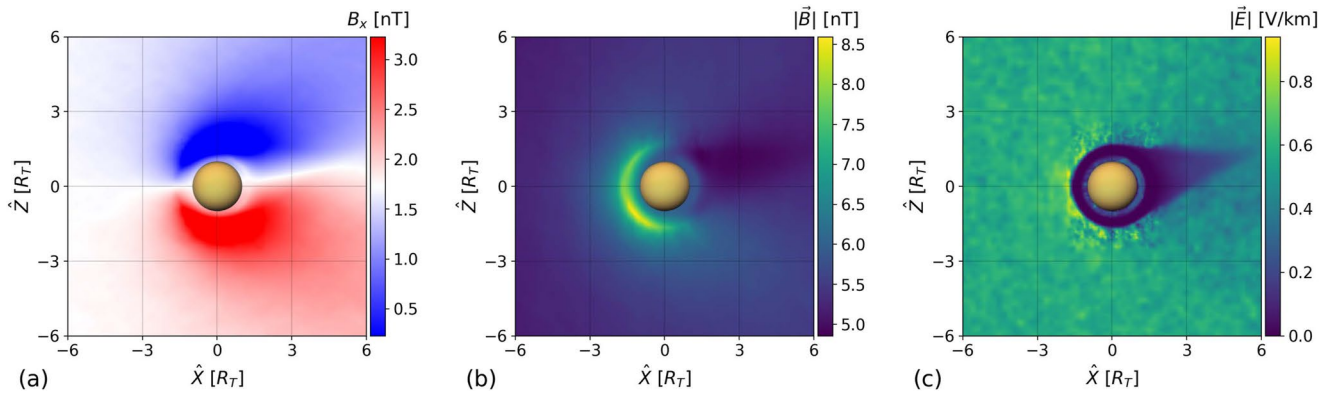


Figure 5. Two-dimensional cuts through Titan's perturbed electromagnetic environment during the TA flyby, determined by the AIKEF hybrid model. Panel (a) shows the B_x component of the magnetic field, that is, the component along the corotational flow direction ($+X$). Here, the background value from Table 1 ($\bar{B}_{0,x} = 1.727$ nT) is colored white. Panels (b, c) display the magnitudes of the magnetic field $|\bar{B}|$ and electric field $|\bar{E}|$, respectively. All three plots show the $\hat{Y} = 0$ plane of the DRAP coordinate system (see, e.g., Figure 1 of Tippens et al., 2022). This plane contains the center of Titan, the background magnetic field vector \bar{B}_0 , and the bulk velocity vector \bar{u}_0 .

the size of the detector in pixels (32×32 in this case) is much larger than size of each pixel Δr and Δs . Since $\mathcal{P}(r, s)$ is a normal distribution, the integral in Equation 14 becomes

$$\int_{-\infty}^{\infty} \int_{-\infty}^{\infty} \mathcal{P}(r, s) ds dr = 1, \quad (15)$$

and we recover the initial ENA flux from the point source that would have hit pixel (r_0, s_0) in an “ideal” instrument: $I = \bar{I}(r_0, s_0)$.

The nominal values for the standard deviations of the PSF in INCA's 24–55 keV channel, which were measured in accelerator tests before Cassini's launch (Krimigis et al., 2004), are shown in Table 2 alongside the values used in two subsequent studies that analyzed INCA data in the same energy range. The nominal values in the first row of Table 2 were determined for 20 keV hydrogen. Since foil scattering at the entrance to the INCA detector decreases as ENA energy increases, these values represent upper limits to $\lambda_{r,s}$ in the 24–55 keV energy channel (Krimigis et al., 2004). In their analysis of INCA images of Titan's hydrogen corona, Brandt et al. (2012) utilized values of $\lambda_{r,s}$ which were calculated for the geometric mean energy (36 keV) of the 24–55 keV channel and are slightly above those from Krimigis et al. (2004). This deviation results from slight changes in the detector characteristics while Cassini was in space. Dialynas et al. (2013) utilized a third set of values for $\lambda_{r,s}$ to study the vertical distribution of Saturn's extended neutral cloud using ENA images.

Due to the evolution of the detector's response over time and the ambiguities associated with determining these changes from in-situ observations, it is not feasible to establish a single definitive PSF for INCA images to be used in post-processing of our synthetic ENA images. For this reason, we will produce multiple synthetic ENA images for TA using each of the three pairs of values for $\lambda_{r,s}$ in Table 2 and treat this as a source of systematic uncertainty in the discussion of our model results. We note that the width of the PSF was also calculated from in-situ data by Mauk et al. (2003), using ENA observations from Cassini's flyby of Jupiter. However, the work of these authors is based on observations from INCA's 55–90 keV hydrogen channel, so their values for $\lambda_{r,s}$ are not applicable to the 24–55 keV channel which acquired the ENA image from TA (Mitchell et al., 2005).

3. Model Results for Titan Flyby TA

3.1. AIKEF Results for Titan's Plasma Environment During TA

Figure 5 shows the AIKEF model results for the perturbed electromagnetic fields in Titan's induced magnetosphere at the time of the TA flyby. An exhaustive discussion of Titan's plasma environment within the framework of the AIKEF model can be found in our preceding publications listed in Section 2.1 (in particular, see Feyerabend et al., 2015, 2016). Therefore, we provide only a brief description of those features that are immediately relevant

to our subsequent analysis of the synthetic ENA images. The upstream parameters used to generate Figure 5 correspond to Case 1 from Table 1, that is, the ambient magnetospheric field vector from the *outbound* leg of the flyby has been used as input for the simulation. Panel 5(a) shows the component of the magnetic field B_x along the corotational flow direction. Panel 5(b) displays the magnetic field magnitude $|\vec{B}|$, and panel 5(c) shows the electric field magnitude $|\vec{E}|$. All three panels display a cross section of the three-dimensional AIKEF domain taken in the $\hat{Y} = 0$ plane of the Draping Coordinate System (DRAP), $\{\hat{X}, \hat{Y}, \hat{Z}\}$, introduced by Neubauer et al. (2006) and subsequently applied by Simon et al. (2013) and Tippens et al. (2022).

The origin of the Cartesian DRAP system is identical to that of the TIIS, and the X axis in the TIIS coincides with the \hat{X} axis in the DRAP system. However, the \hat{Y} and \hat{Z} axes of the DRAP system are rotated around the $X = \hat{X}$ axis, such that the $\hat{Y} = 0$ plane contains both the upstream plasma velocity \vec{u}_0 and the background magnetic field vector \vec{B}_0 . This rotation eliminates the $B_{0,y}$ component of the background magnetic field. Hence, the draped magnetic field lines near Titan are (mostly) parallel to the $\hat{Y} = 0$ plane (e.g., Simon et al. 2007a, 2007b). In the DRAP system, the ambient convective electric field $\vec{E}_0 = -\vec{u}_0 \times \vec{B}_0$ is antiparallel to the \hat{Y} axis. Therefore, Titan's "flat" tail of ionospheric pick-up ions is confined close to the $\hat{Z} = 0$ plane (e.g., Simon & Motschmann, 2009). In other words, the DRAP system allows for a straightforward analysis of the plasma and field perturbations generated by Titan's magnetospheric interaction (such as the pick-up tail or the magnetic draping pattern). The DRAP coordinates used in Figure 5 are rotated from the TIIS by 38.9° . For a visualization of the relationship between the DRAP and TIIS systems, see, for example, Figure 1 in either Simon et al. (2013) or Tippens et al. (2022).

Major features of Titan's super-Alfvénic ($M_A = 1.65$), sub-magnetosonic ($M_{MS} = 0.75$) interaction with Saturn's magnetospheric plasma are visible in the AIKEF output (Figure 5). The magnetospheric field lines drape around the moon, forming a pair of Alfvén wings that are strongly inclined against the background field (Figure 5a). The draping causes the B_x component to be reduced (colored blue) in the $\hat{Z} > 0$ half space and enhanced (colored red) in the $\hat{Z} < 0$ half space. Because the background magnetic field \vec{B}_0 has a positive $B_{0,x}$ component (white in Figure 5a; see Table 1), the perturbed B_x component in the $\hat{Z} > 0$ wing remains positive (see also Simon & Motschmann, 2009). The tilt of the ambient magnetospheric field toward downstream (by about 20°) also causes the interaction to be slightly asymmetric between the $\hat{Z} > 0$ and $\hat{Z} < 0$ half spaces: within the plane shown in Figure 5, the draping pattern is rotated around Titan in counter-clockwise direction. This rotation also manifests in the location of the magnetic neutral region downstream of the moon, which is "lifted" to slightly above the $\hat{Z} = 0$ plane (white in Figure 5a, see also Simon & Motschmann, 2009).

Figure 5b shows the magnetic pile-up region upstream of Titan (colored yellow) generated through mass-loading of the plasma by newly generated ionospheric ions. These ions locally slow the bulk flow, causing the magnetospheric field lines to pile up, leading to an enhancement in the field strength of up to 76% compared to the background value of $B_0 = 4.98$ nT (dark blue in Figure 5b). Since the convective electric field $\vec{E} = -\vec{u} \times \vec{B}$ depends on the bulk plasma velocity \vec{u} , this mass-loading lowers the field magnitude $|\vec{E}|$ in Titan's ionosphere and in the downstream tail region, which are both dominated by slow heavy ions. This can be seen in Figure 5c as the dark blue region. The pick-up ions gyrate perpendicular to the $\hat{Y} = 0$ plane shown in Figure 5 and form an asymmetric tail that expands into the $\hat{Y} < 0$ half space by about $3 R_T$ (see, e.g., Feyerabend et al., 2015; Simon & Motschmann, 2009).

The plasma and field perturbations shown in Figure 5 present similarly for Case 2 from Table 1, using magnetic field data from the *inbound* region of TA to calculate \vec{B}_0 . In Case 2, the background field magnitude is 17% higher than in Case 1, causing the Alfvén wings (blue and red regions in Figure 5a) to be slightly less inclined. Ion gyroradii are decreased by only about 15%. The background magnetic field \vec{B}_0 is inclined against the $(-\hat{Z})$ axis by about 8° in the inbound case compared to 20° for the outbound case, implying that the neutral region downstream of the moon remains closer to the $\hat{Z} = 0$ plane for Case 2. Thus, the important features in Titan's plasma interaction—such as the field draping and the pick-up tail—are very similar between Cases 1 and 2.

Figure 6 shows the time series of the electron number density along Cassini's trajectory during TA. The black line is the number density produced by AIKEF (corresponding to the total ion number density at the respective location), and the colored points represent values measured by two Cassini instruments: the CAPS electron spectrometer (blue dots), and the Langmuir probe (LP) of the Radio and Plasma Wave Science (RPWS) instrument suite (red dots). Data from both instruments are shown here because CAPS was more suitable for measuring the density of the magnetospheric plasma, while the LP was designed to detect the cold plasma in Titan's ionosphere

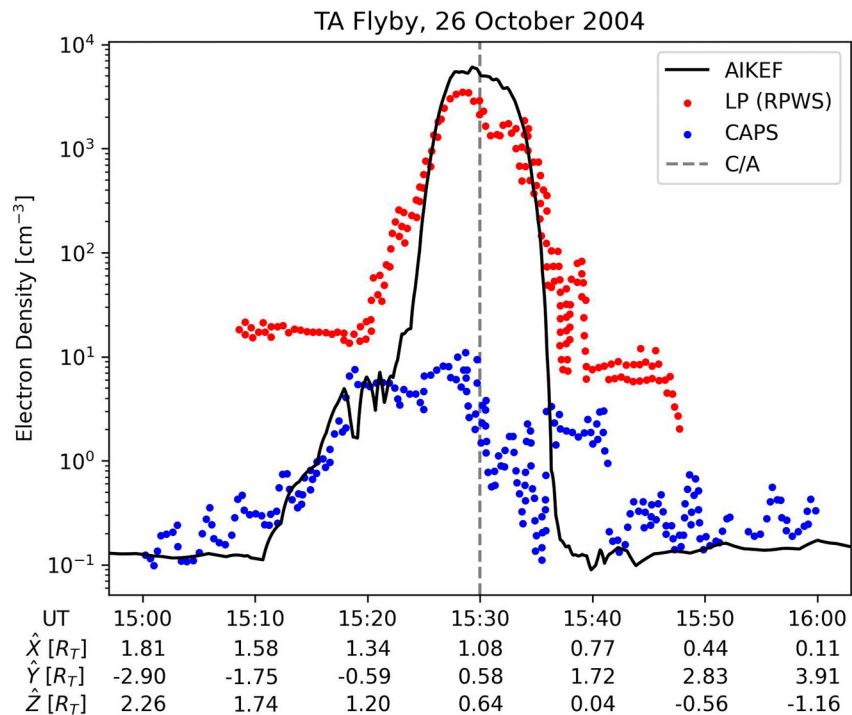


Figure 6. Observed and modeled electron density along Cassini's trajectory during the TA flyby of Titan. The values measured by the spacecraft are shown in blue (from CAPS) and red (from the Langmuir Probe of the RPWS instrument suite). The observed time series have been extracted from Figure 6 of Ma et al. (2006). The modeled electron density from AIKEF is shown in black. The horizontal axis is labeled in increments of 10 min around closest approach at 15:30 UT (C/A, indicated by the vertical dashed gray line). The position coordinates of the spacecraft at these times are given in the DRAP coordinate system $\{\hat{X}, \hat{Y}, \hat{Z}\}$.

(Gurnett et al., 2004; Ma et al., 2006; Young et al., 2004). This difference in instrument characteristics also explains the offset between the electron number densities measured by CAPS and the LP outside of Titan's ionosphere visible in Figure 6 (before 15:20 UT and after 15:40 UT).

The modeled density along the TA trajectory qualitatively and quantitatively reproduces numerous key features of the time series measured by Cassini. In the thermal magnetospheric plasma (up to 15:20 UT and after 15:40 UT), the model results agree with the electron densities from CAPS, while within Titan's ionosphere (between 15:20–15:40 UT) the model is consistent with measurements from the LP. The location of the ionospheric electron density maximum in AIKEF (around 15:29 UT) coincides with the position of the maximum value measured by the LP. Along the TA trajectory, Cassini encountered the maximum electron density around 1,030 km altitude. From their analysis of the T83–T88 flybys, Edberg et al. (2013) concluded that Cassini remained above the altitude of Titan's peak ionospheric density during TA. The maximum electron density in AIKEF exceeds the observed value by about a factor of 1.4. Given the uncertainties in the upstream flow conditions (see Section 2.1), Figure 6 demonstrates that AIKEF can adequately describe the perturbations in Titan's plasma environment at the time of TA. We note that our model reproduces the observed electron densities equally well using the upstream magnetic field from Case 2 in Table 1.

Within the ionosphere, both the modeled densities and those observed by the LP are largely symmetric about closest approach (C/A, dashed line in Figure 6). However, while the modeled density displays a single broad peak, the measured time series reveals a “double peak” structure with the density being 2–3 times higher before C/A than after. The broad peak in our modeled electron density is consistent with modeling of Titan's ionosphere during TA performed by Cravens et al. (2005), who also included solar UV and electron impact ionization. The agreement between these two models may imply that the “splitting” of the observed density maximum was caused by non-stationary processes in Titan's ionosphere near the TA trajectory that are captured by neither approach. Farther from the moon both our modeled density and the profile from CAPS are asymmetric about closest approach between the $\hat{Y} > 0$ and $\hat{Y} < 0$ half spaces: the density from 15:10–15:19 UT approaches an

order of magnitude higher than from 15:40–15:50 UT. The “rising edge” in density between around 15:10 and 15:19 UT revealed by CAPS observations is also visible in the AIKEF results. This asymmetry may be partially caused by the slight inclination of Cassini’s trajectory toward upstream (see Figure 1). However, results from the AIKEF model also suggest the electron densities in Titan’s pick-up tail to be asymmetric between the $\hat{Y} < 0$ and $\hat{Y} > 0$ half spaces (e.g., Feyerabend et al., 2015). The newly generated pick-up ions initially travel into the $\hat{Y} < 0$ half space on cycloidal trajectories with gyroradii $R_g \approx 3R_T$, since in that region the convective electric field points away from the moon. For this reason, the plasma density is expected to be elevated in the $\hat{Y} < 0$ half space compared to $\hat{Y} > 0$. Our model results (black line in Figure 6) suggest that Cassini sampled this region of increased electron density in the $\hat{Y} < 0$ half space during the inbound leg of TA.

We note that we did not find a set of upstream parameters that simultaneously explains the observed electron densities and data from Cassini’s ion spectrometer (e.g., Hartle et al., 2006) or magnetometer (e.g., Backes et al., 2005). This may suggest that the non-stationarities observed in Titan’s magnetospheric environment during TA (Simon et al., 2010a, 2010b) did affect the structure of the moon’s interaction region at the time of the flyby. Time variations in the ambient magnetospheric field during the flyby will be considered as a source of uncertainty in the interpretation of our synthetic ENA images. So far, only the MHD model of Ma et al. (2006) was able to simultaneously reproduce the time series of both electron density and magnetic field from TA. However, in order to achieve this, the authors had to tilt the upstream flow velocity \vec{u}_0 away from the (+X) axis by about 23°. The inclusion of upstream flow components away from the corotation direction, in addition to the background magnetic field being tilted against the (−Z) axis, would significantly complicate the interpretation of our modeled ENA images. Therefore, we have decided against taking such a step.

3.2. Synthetic ENA Images in Uniform and Draped Fields

Figure 7 shows ENA images for the TA flyby: panel 7(a) is the actual ENA image taken by INCA and panels 7(b) and (c) are synthetic ENA images generated by our model. The integration period of the observed image is from 15:04 UT to 15:13 UT (green segment of the trajectory in Figure 1), while both synthetic images are determined for the detector’s location and pointing at the midpoint of this period (15:08 UT, orange dot in Figure 1). Panel 7(b) displays the synthetic ENA image produced by parent ions moving through uniform fields, while panel 7(c) shows the synthetic image generated by ions moving through the draped fields from AIKEF. In the uniform field case, the electric field is purely convective and is given by $\vec{E}_0 = -\vec{u}_0 \times \vec{B}_0$. Both synthetic ENA images have been generated using the PSF parameters from Krimigis et al. (2004), see top row of Table 2. The role of the PSF in shaping the modeled ENA images will be investigated in Section 3.3. We do not use the observed ENA image from TA shown in either Mitchell et al. (2005) or Wulms et al. (2010) because those images had additional smoothing applied to them. Instead, using the unprocessed image in panel 7(a) facilitates comparison with the two synthetic images, which are obtained from the model (Sections 2.2 and 2.3) without additional artificial steps that may smear out or eliminate small-scale features.

All three images are displayed in the “skymap” azimuthal projection used in preceding publications on ENA observations from Titan (e.g., Brandt et al., 2012; Dialynas et al., 2013; Mitchell et al., 2005); lines of constant detector azimuth and elevation are denoted by dashed lines and Titan’s surface by the solid circle. During the integration period, the elevation axis of the detector plane was rotated clockwise against the (+Z) axis of the TIIS system by about 90°. Therefore, in the images from Figure 7 detector elevation is shown on the horizontal axis and detector azimuth increases downward on the vertical axis. As indicated by the black arrows pointing northward and southward, the (+Z) axis of the TIIS approximately points toward the top of each image. Due to INCA’s orientation during the integration period (Figure 1), the right side of these images (positive detector elevation) primarily shows the region downstream ($X > 0$) of Titan while the left side (negative detector elevation) captures the upstream ($X < 0$) region.

Figure 7a shows the familiar crescent pattern of elevated ENA flux in the INCA image from TA. A few pixels are heavily saturated due to noise, and some are likely affected by ENAs from sources other than Titan (such as Saturn’s atmosphere). The observed crescent is largely composed of ENA fluxes between 3 and 8 [cm² sr s keV]^{−1}. It wraps around the downstream hemisphere of Titan, reaching below the southern pole and extending somewhat beyond the northern pole, with the opening of the crescent residing upstream of the moon. A simple picture of the mechanism generating this crescent can already be obtained by treating the magnetospheric field near Titan as uniform (pointing southward) and considering only the gyration (but not the drift motion) of the parent protons

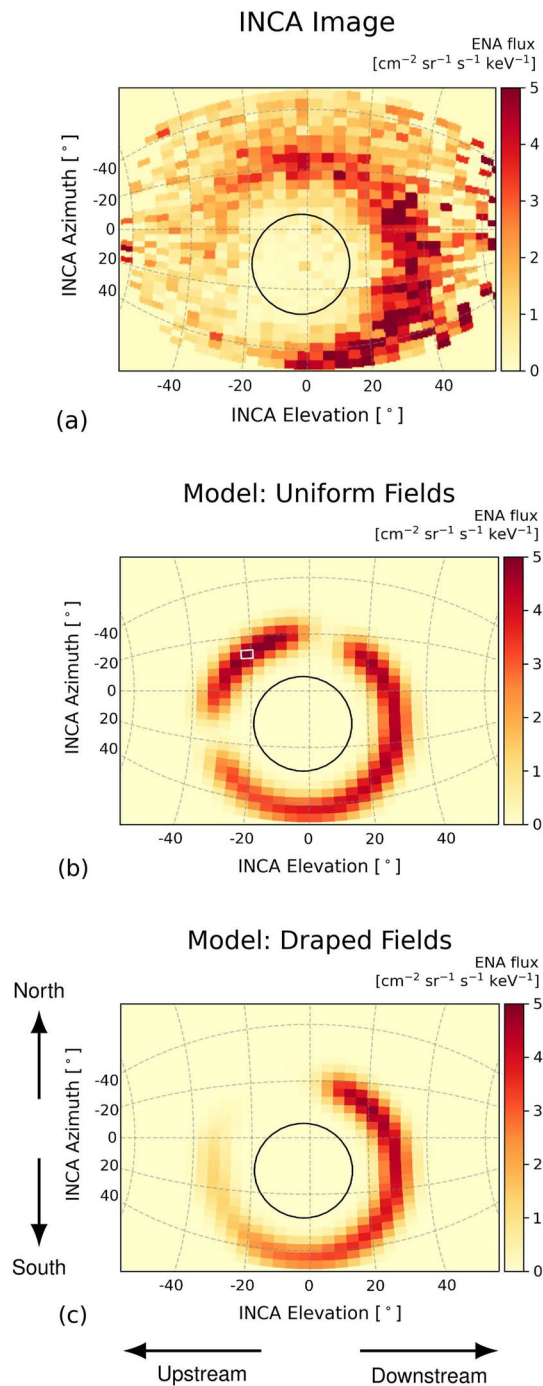


Figure 7. Observed and synthetic ENA images for Cassini's TA flyby of Titan. Titan's disk is represented by the black circle. Panel (a) shows unprocessed INCA data obtained using the XINCA tool available at http://cassini-mimi.jhuapl.edu/xinca_v17.html. The pixel values in the observed image are averaged over an integration period from 15:04 to 15:13 UT (colored green in Figure 1). Panels (b, c) display synthetic ENA images produced by our model for INCA's location and pointing at the middle of this integration period (15:08 UT, orange dot in Figure 1). Panel (b) shows the synthetic ENA image generated by tracing the parent ions through the uniform magnetospheric background fields, and panel (c) shows the synthetic image obtained using the draped fields from AIKEF. The white square in panel (b) indicates a pixel where the sample parent ion shown in the left column of Figure 8 contributes to the modeled ENA flux. All three images are represented in the "skymap" azimuthal projection, with detector elevation and azimuth denoted by dashed lines. The detector elevation is along the horizontal axis and the detector azimuth appears reversed due to the (approximately) 90° clockwise rotation of the INCA detector against the (+Z) axis of the TIIS. The black arrows indicate the approximate locations of north, south, upstream, and downstream in these images.

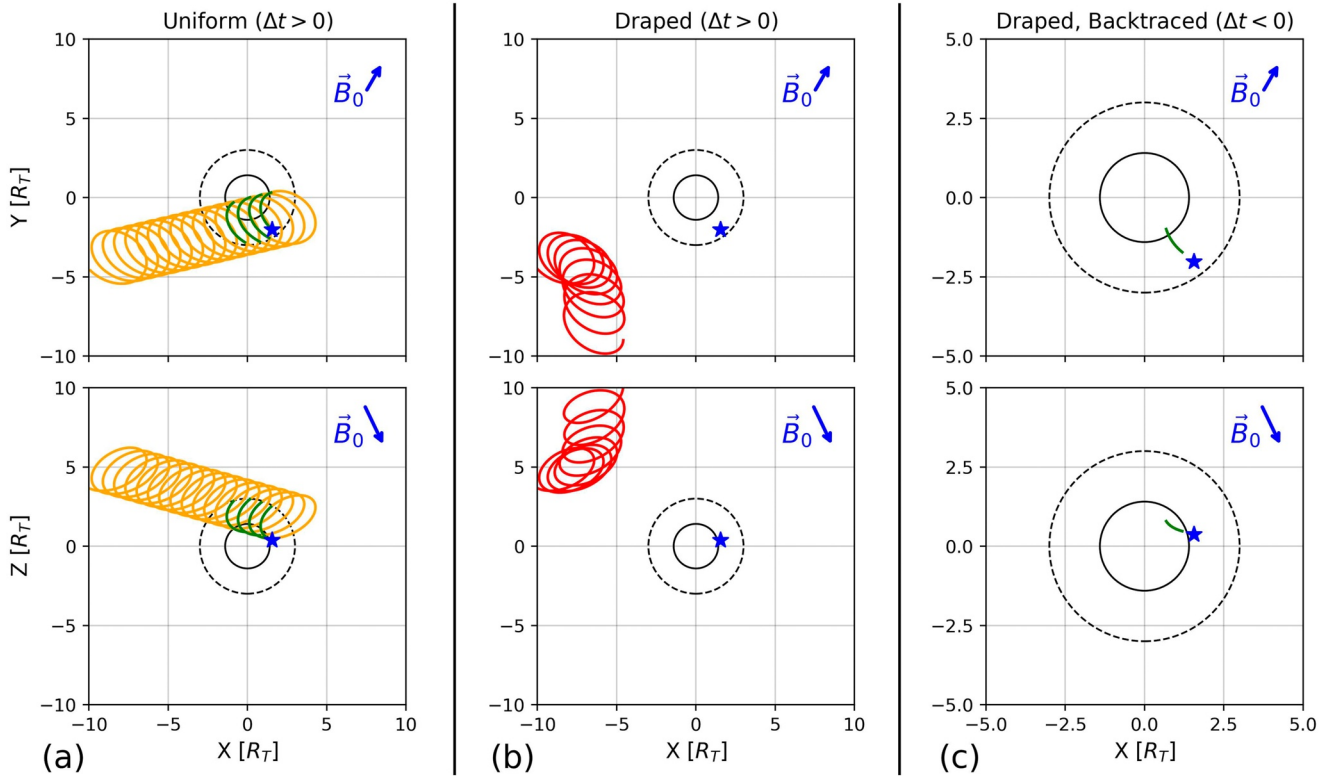


Figure 8. Example energetic parent proton trajectories demonstrating how field line draping depletes the ENA flux into the opening of the observed crescent pattern. The position of the model detector is indicated by the blue star. The trajectory of the ion moving through uniform fields is colored orange, and trajectories in draped fields are colored red when they are outside of Titan's atmosphere. All trajectories are colored green where they reside inside the atmosphere (indicated by the dashed circle), that is, where they produce ENAs. The solid inner circle represents the MPD at an altitude of $0.4 R_T$. The top row displays the trajectories projected onto the $Z = 0$ plane and the bottom row shows the projection onto the $Y = 0$ plane of the TIIS. The background magnetic field vector \vec{B}_0 is shown in blue, projected onto the respective plane. Columns (a, b) show ions which are traced forward in time ($\Delta t > 0$), while column (c) shows an ion which is backtraced ($\Delta t < 0$). Column (a) contains the trajectory of a parent proton which, in uniform fields, emits ENA flux into a pixel of the high flux region in the opening of the crescent feature (white square in panel 7(b)). This ion is launched at position $\vec{x} = \{-10.00, -4.51, 3.66\} R_T$ with initial velocity $\vec{v} = \{1659, -1787, -826\}$ km/s and initial energy $E_0 = 34.6$ keV. Column (b) shows the trajectory of a proton launched outside of Titan's interaction region with the exact same initial conditions, but which travels forward in time through draped fields. Column (c) displays the backtraced trajectory of a parent ion which is launched from the exact point where the ion trajectory in column (a) terminates, that is, where it emits an ENA toward the highlighted (white square) pixel of the detector. Its initial conditions are $\vec{x}_0 = \{1.65, -2.09, 0.35\} R_T$ and $\vec{v}_0 = \{1967, -1601, -522\}$ km/s, corresponding to an energy of $E = 35.0$ keV. In contrast to the ion in column (a), the particle displayed in column (c) is traced through draped fields and passes below the MPD shortly after launch, that is, its trajectory is forbidden. In uniform fields, the proton trajectory backtraced from this location would be identical to the trajectory traced forward in time in column (a).

in this field (see also, e.g., Mitchell et al., 2005). In the upstream hemisphere, the gyrating protons move toward the spacecraft outside of the moon's atmosphere and away from the spacecraft inside of the atmosphere; that is, the newly generated ENAs can not reach the detector. In the downstream hemisphere, the situation is reversed: the gyrating protons move toward the spacecraft while inside of Titan's atmosphere, thereby generating ENAs that can be detected. The altitude of the inner edge of the crescent can be calculated using the detector's pointing and its position relative to Titan. We find the crescent's inner edge to be located around 1,400 km altitude, that is, near Titan's exobase (Regoli et al., 2016) and just below the altitude of maximum ENA production (Tippens et al., 2022). The gap between the moon's disk and the ENA crescent supports the notion of the MPD as an inner boundary for detectable ENAs, and indicates that an MPD altitude of 1,045 km is sufficiently conservative to model ENA observations.

Our model produces synthetic ENA images within the same intensity range as the observed images: the regions of elevated flux in the modeled images contain ENA fluxes between around $3\text{--}5$ $[\text{cm}^2 \text{sr s keV}]^{-1}$. In both uniform and draped fields, the modeled ENA emission pattern reveals the expected, crescent-like morphology above Titan's downstream hemisphere (panels 7(b) and (c)). However, when the ambient fields are treated as uniform there is an additional "island" of elevated ENA flux (containing the pixel highlighted by the white box) in the opening of the crescent pattern above Titan's northern upstream hemisphere. Similar to the crescent, this region of elevated flux

forms a segment of a circle around Titan's disk; however, it is isolated from the crescent by a region of nearly zero ENA flux at either end. This isolated feature contains the highest ENA flux values in the synthetic ENA image for uniform fields, reaching $5.2 \text{ [cm}^2 \text{ sr s keV]}^{-1}$ compared to a maximum of $4.8 \text{ [cm}^2 \text{ sr s keV]}^{-1}$ in the crescent (panel 7(b)). The existence of this feature in uniform fields demonstrates the importance of the parent ions' drift motion and their origins in the ambient plasma for determining the ENA emission pattern. The models of Dandouras and Amsif (1999) and Mitchell et al. (2005), which initialize ions everywhere around Titan and consider gyration alone, do not predict it. In both uniform and draped fields, the inner edge of our modeled crescent (panels 7(b) and (c)) is located at around the same 1,400 km altitude as in the observed image (panel 7(a)), but the observed crescent is broader than in the modeled images. Toward downstream, the outer edge of the crescent reaches $40\text{--}45^\circ$ elevation in the observed image, while in both model images it extends to only around 35° elevation. In uniform fields (panel 7(b)), the crescent pattern on the downstream side has nearly the same intensity as in the draped case (panel 7(c)).

The crescent pattern in both modeled ENA images is somewhat rotated in clockwise direction, compared to the pattern in the observed image which is more symmetric with respect to Titan's equator. Below the moon's south polar cap, the crescent in the observed image (panel 7(a)) is largely confined to the downstream hemisphere. In the modeled image for draped fields (panel 7(c)), the region of elevated ENA flux extends beyond the south pole into the upstream hemisphere. The intensity gradually decreases when approaching Titan's equator from below. In uniform fields (panel 7(b)), the ENA flux intensity below Titan's south polar cap is elevated up to around 25° azimuth, where it cuts off more sharply than in draped fields. Conversely, the crescent in the observed ENA image wraps around Titan's *north* polar cap where it extends into the upstream hemisphere (panel 7(a)). In both synthetic images, the crescent does not reach the north pole, extending only to about 5° elevation in the downstream hemisphere (panels 7(b) and (c)). The time variability of the observed ambient magnetospheric field vector during TA led to changes in the orientation of the protons' gyroplanes over the course of the flyby: these planes rotated with the magnetic field vector, even during the 9 min integration period (see, e.g., Neubauer et al., 2006). This time-dependence of the background field influences the precise size and location of the ENA emission crescent in the observed image (as we will discuss in Section 3.3), but it is not reflected in the two synthetic images in Figure 7. Nonetheless, the model setup using draped fields from AIKEF both qualitatively and quantitatively reproduces the prominent features of the actual ENA image taken during TA, namely the crescent pattern with maximum flux on the downstream side and a gap in flux on the upstream side of Titan (panels 7(a) and (c)).

Comparing panels 7(b) and 7(c) highlights the influence of the field line draping on Titan's ENA emission signature. The isolated ENA emission feature in the opening of the crescent is entirely absent when draping is considered (panel 7(c)). The isolated feature is also absent in the observed image. Thus, we can reproduce the major features of the observed ENA flux pattern only when taking into account the draping of Saturn's magnetospheric field around Titan: without the field draping, the modeled flux pattern forms an "interrupted ring" structure, rather than the observed crescent pattern.

The example energetic parent proton trajectories in Figure 8 illustrate how field line draping causes the differences between the two synthetic ENA images (panels 7(b) versus (c)). The top and bottom rows display proton trajectories projected onto the $Z = 0$ and $Y = 0$ planes of the TIIS, respectively. Each of the three columns shows a different parent ion trajectory. The trajectories in columns (a) and (b) were generated separately from the backtracing model to illuminate the effect of field line draping and are traced *forward* in time, while the trajectory in column (c) was backtraced by our ENA model. The proton in column 8(a) is launched upstream of Titan and is propagated forward in time through uniform magnetospheric fields. While this macroparticle gyrates and drifts toward downstream, one of the ENAs it emits travels along the detector LOS of the pixel at approximately -20° elevation and -14° azimuth (outlined by the white square in Figure 7b). In this way, it contributes to the region of high ENA flux that is isolated from the crescent in Figure 7b.

Column 8(b) shows the trajectory of a parent ion which is launched with the exact same initial conditions as the one shown in column 8(a). However, this particle is traced forward in time through the draped fields produced by AIKEF (see Figure 5). As it drifts toward Titan, it approaches the upstream flank of the moon's ramside pileup region and is deflected into the ($Z > 0$, $Y < 0$) quadrant, so that it never enters the moon's atmosphere. This particular ion is redirected by the magnetic field enhancement along the upstream flank of Titan's pick-up tail, which is stretched into the ($Y < 0$) half space (see also, e.g., Simon et al., 2007b). We have identified numerous other parent ions with similar trajectories: in uniform fields, these would emit ENAs toward the isolated feature

in the upper left quadrant of Figure 7b, whereas in draped fields they do not contribute to the ENA image at all. Deflection of energetic ions by the pile-up region upstream of Titan (and along the Saturn-averted flank of its pick-up tail) thus contributes to the disappearance of the isolated region of high ENA flux when switching from uniform to draped fields (panel 7(b) versus 7(c)).

Column 8(c) displays the trajectory of a parent proton which is launched from the same point where the ion from column 8(a) emitted its observable ENA into the detector pixel at -20° elevation and -14° azimuth. It is initialized at the end of the pictured trajectory nearest to the detector (indicated by the blue star in Figure 8) with the same velocity vector as the ENA which is emitted into the detector (in uniform fields) by the parent ion shown in column 8(a). However, the ion in column 8(c) is traced *backwards* in time. While the forward-traced trajectories in columns 8(a) and 8(b) reveal a possible physical mechanism for the disappearance of the isolated ENA emission feature, our model generates the synthetic images by tracing parent ions backwards in time ($\Delta t < 0$). We include the ion trajectory in column 8(c) to demonstrate how the isolated emission feature in panel 7(b) is eliminated when field line draping is included within the context of our detector model. In uniform fields the (backtraced) parent proton in column 8(c) would follow the *same* trajectory as the ion from column 8(a). However, soon after it is launched in *draped* fields (column 8(c)), this ion approaches the region of enhanced fields in Titan's northern hemisphere (see Figure 5b) from below and is deflected back toward the moon. It encounters the MPD, meaning that it possesses a forbidden trajectory and cannot contribute ENA flux along this LOS. The draped fields at Titan thus make this LOS, and those of its neighboring pixels, largely inaccessible to energetic parent ions, resulting in little to no ENA flux toward the opening of the crescent pattern in Figures 7a and 7c.

The synthetic ENA image for draped fields in Figure 7c is similar to the ENA emission maps produced by Wulms et al. (2010) for TA using a plane detector and draped fields from an MHD model (see right column of Figure 15 therein). In their study as well as ours, the field draping is necessary to obtain the observed crescent morphology on the downstream side of Titan. However, Wulms et al. (2010) found that in uniform fields the crescent pattern was mirrored compared to the draped case, with the greatest ENA flux in the equatorial upstream region and with the gap in the crescent downstream of Titan. In contrast to this, our results suggest that the *location* of the crescent is *nearly the same* in uniform and draped fields. However, in the uniform case our modeled crescent is augmented by the isolated region of enhanced flux (see Figure 7b). There are two possible contributors to these differences: first, we use a background magnetic field vector that is rotated by 13° against that in the MHD model used by Wulms et al. (2010). We will investigate the influence of the chosen background field vector on our synthetic images in Section 3.3. Second, both models apply different approaches to select the velocity vectors of ENAs which contribute to the images: all ENAs reaching the plane detector of Wulms et al. (2010) travel in nearly the same direction (approximately antiparallel to the detector's normal vector); while in our model the ENA velocity vectors converge on the point-like detector location.

The model used by Kabanovic et al. (2018), like that of Wulms et al. (2010), generated ENA emission maps using a plane detector. However, these authors traced parent ions through draped fields produced by the AIKEF hybrid model, which we also employ in our study. The ENA morphology in draped fields obtained by Kabanovic et al. (2018) for TA is qualitatively different from our synthetic image (see Figure 11d therein versus our Figure 7c). The ENA emission pattern computed by Kabanovic et al. (2018) for TA contains two isolated regions of enhanced flux above Titan's polar caps, with gaps of near-zero flux separating them at mid-to-low latitudes both downstream and upstream. The pattern seen by those authors in uniform fields reveals largely the same morphology as in their draped case but with greater intensity. Thus, their modeled emission patterns are also distinct from the output of our model for both uniform and draped fields (panels 7(b) and (c)). The differences between our modeled ENA images and the ENA flux maps produced by Kabanovic et al. (2018) emphasize the importance of a realistic detector geometry for modeling ENA observations from Cassini's Titan flybys.

3.3. Sensitivity of Synthetic ENA Images to Model Parameters

In this section we investigate two sources of uncertainty in the synthetic ENA images produced by our model (see Figures 7b and 7c): our choice of the PSF for the INCA detector (see Table 2), and the ambient magnetic field vector, which changed in both direction and magnitude over the course of the TA flyby (Neubauer et al., 2006). We first address the effect of the chosen PSF. Figure 9 shows synthetic ENA images for TA in draped fields, again generated using the ambient plasma parameters from Case 1 (see Section 2.1). Each of the three images in panels 9(a) through (c) uses a different pair of values $\lambda_{r,s}$ for the standard deviations of the PSF (see Equation 9

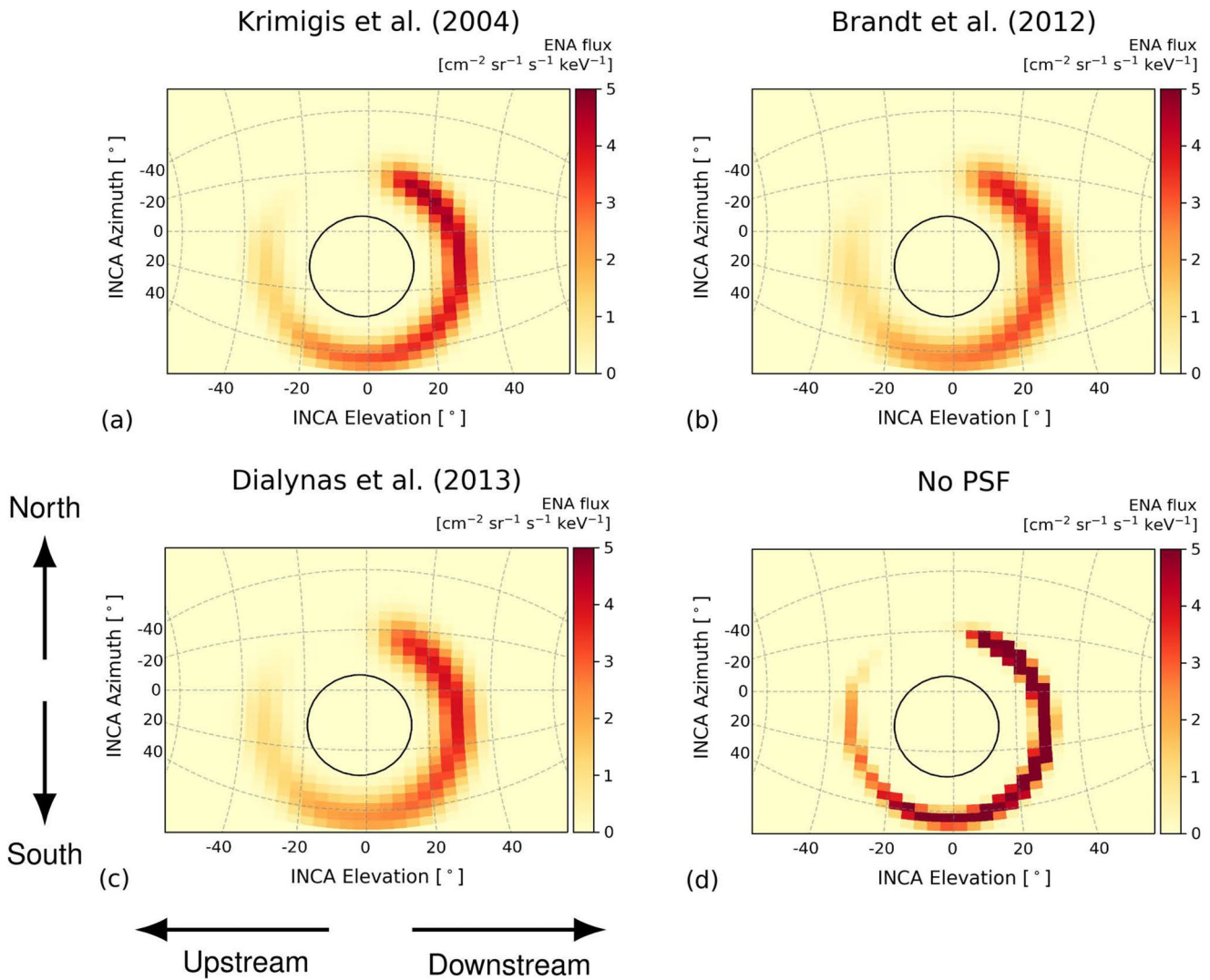


Figure 9. Synthetic ENA images for the TA flyby, generated using the three different PSFs from Table 2. The plots are formatted in the same manner as in Figure 7. All four images use the electromagnetic fields from the same AIKEF run (Case 1 in Table 1) and display the ENA emission morphology in draped fields. Panel (a) shows the synthetic ENA image using the PSF parameters from Krimigis et al. (2004); this image is the same as shown in Figure 7(c). Panels (b, c) display the ENA images obtained by using the parameters $\lambda_{r,s}$ from Brandt et al. (2012) and Dialynas et al. (2013), respectively. To establish a baseline for our analysis, panel (d) shows the modeled ENA image with no PSF applied.

and Table 2). Panel 9(a) shows the modeled TA image using the PSF parameters from Krimigis et al. (2004); this image is identical to the one in Figure 7c and is shown here again to facilitate comparison. Panels 9(b) and (c) display the same output of the particle tracing model with the PSF parameters from Brandt et al. (2012) and Dialynas et al. (2013) applied, respectively. To illustrate the impact of the PSF on the output of the particle tracer, panel 9(d) shows the model output with no PSF applied at all. In other words, panel 9(d) illustrates the distribution of the ENA flux seen by an “ideal” detector, where the image is not smeared out by detector effects. All three images in panels 9(a)–(c) would look the same as the image in panel 9(d) if no PSF was considered.

When a PSF is applied, the three modeled ENA images are very similar, revealing only minor quantitative differences between them (panels 9(a)–(c)). The crescent pattern of elevated ENA flux is present with nearly the same width and angular extension around Titan across all three images. It reaches just downstream of 0° detector elevation over Titan’s northern polar cap, with a “tail” of lower flux that wraps around the southern polar cap into the low latitudes of the moon’s upstream hemisphere. The values for $\lambda_{r,s}$ provided by Krimigis et al. (2004) are slightly lower than those from the other two studies (see Table 2). The width of the Gaussian bell defining the PSF is thus smaller, that is, the crescent is slightly more confined and less “washed out.” For this reason, the average

flux values in the crescent are around 12% and 20% higher in panel 9(a) than in panels 9(b) and (c), respectively. The highest ENA flux in these three modeled images, found in the northern downstream portion of the crescent, is 18%–20% higher in panel 9(a) compared to panels 9(b) and (c).

The values for $\lambda_{r,s}$ used by Brandt et al. (2012) and Dialynas et al. (2013) are similar, with the former being slightly larger in elevation (λ_r) and the latter being greater in azimuth (λ_s). As a result, the modeled crescent features in panels 9(b) and (c) are nearly indistinguishable, with the ENA flux intensity in panel 9(c) being less than 2% greater on average. The highest ENA flux value in panel 9(c) is only 2% greater than the peak flux in panel 9(b). Panels 9(a) through (c) indicate that, within the documented range of values for the width of the PSF, our choice of $\lambda_{r,s}$ influences the modeled ENA emission morphology only quantitatively. In the following, we therefore continue to use the parameters from Krimigis et al. (2004) for our synthetic ENA images.

By contrast, the synthetic ENA image in panel 9(d), which has had no PSF applied to it, shows a much narrower ENA crescent than panels 9(a)–(c) and possesses the highest ENA fluxes within the entire series of model runs. A comparison to the actual observations from TA (Figure 7a) indicates that, without the PSF applied, the modeled image would severely overestimate the magnitude of the ENA flux in the crescent while underestimating its (radial) width. However, panel 9(d) also illustrates that application of the PSF does *not* change the morphology of the synthetic ENA images; only the intensity of the incoming flux is redistributed.

We next investigate the sensitivity of our modeled ENA images to our choice of the ambient magnetic field vector. Figure 10 shows the synthetic ENA images produced in both uniform and draped fields for the two different background magnetospheric field vectors provided in Table 1: the modeled images in the left column (panels 10(a) and (c)) were generated using the averaged magnetic field from the outbound region of TA (Case 1), whereas the average field from the inbound region (Case 2) is used in the right column (panels 10(b) and (d)). The orientations of these two field vectors differ by 33°, with magnitudes of $B_{0,1} = 4.98$ nT on the outbound leg and $B_{0,2} = 5.85$ nT on the inbound leg. The top row (panels 10(a) and (b)) contains our modeled images for uniform fields and the bottom row (panels 10(c) and (d)) displays the images for the draped fields from AIKEF. Figures 10a and 10c are identical to Figures 7b and 7c, respectively. We show them here again to facilitate comparison with the modeled images for Case 2. All four images in Figure 10 were produced for the detector location and pointing during TA, as shown in Figure 1.

In uniform fields, the model run for Case 2 (panel 10(b)) produces a similar “segmented circle” pattern of elevated ENA flux as the Case 1 setup (panel 10(a)). However, in Case 2 the segment of elevated flux above Titan’s northern polar cap is nearly the same size as the one below the southern polar cap. In contrast to Case 1 (panel 10(a)), *both* polar caps are now “covered” by regions of elevated ENA flux. These two segments are separated by gaps of near-zero ENA flux in the equatorial upstream hemisphere and at low northern latitude in the downstream hemisphere. Thus, even when treating the magnetic field near Titan as uniform, switching from the ambient field vector $\vec{B}_{0,1}$ observed on the outbound leg to that of the inbound leg ($\vec{B}_{0,2}$) does have a clearly discernible impact on the synthetic ENA image for TA (panels 10(a) and (b)).

The modeled ENA flux patterns in draped fields (panels 10(c) and (d)) are qualitatively distinct from one another. When the inbound magnetic field vector $\vec{B}_{0,2}$ is used (Case 2, see panel 10(d)), an isolated segment of elevated ENA flux (again containing the pixel highlighted in white) is still present above Titan’s northern upstream hemisphere when the fields are draped. This is a key difference from the ENA emission morphology for Case 1 (panels 10(a) and (c)), where this isolated flux segment is eliminated when field line draping is included. Compared to uniform fields (panel 10(b)), in Case 2 both segments of increased ENA flux are shrunken in the “draped fields” scenario (panel 10(d)), with the gaps of near-zero ENA flux in the upstream equatorial region and at mid-latitudes downstream having grown in angular extension. In draped fields, the crescent of elevated ENA flux in Case 1 (panel 10(c)) wraps most of the way around the moon and possesses the highest flux values in the downstream northern hemisphere. However, in Case 2 (panel 10(d)) this feature covers only Titan’s southern polar cap. The intensity of the ENA flux within the elevated flux regions is still similar between Cases 1 and 2 (panels 10(c) and (d)), analogous to the results for uniform fields.

To understand why the isolated flux segment in the northern hemisphere persists in draped fields for the inbound case (using $\vec{B}_{0,2}$) but is absent for the outbound case (using $\vec{B}_{0,1}$), we examine two additional parent ion trajectories. Figure 11 shows energetic proton trajectories that have been backtraced through uniform (column (a)) and draped (column (b)) fields. Both setups use the background magnetic field vector $\vec{B}_{0,2}$ observed during the

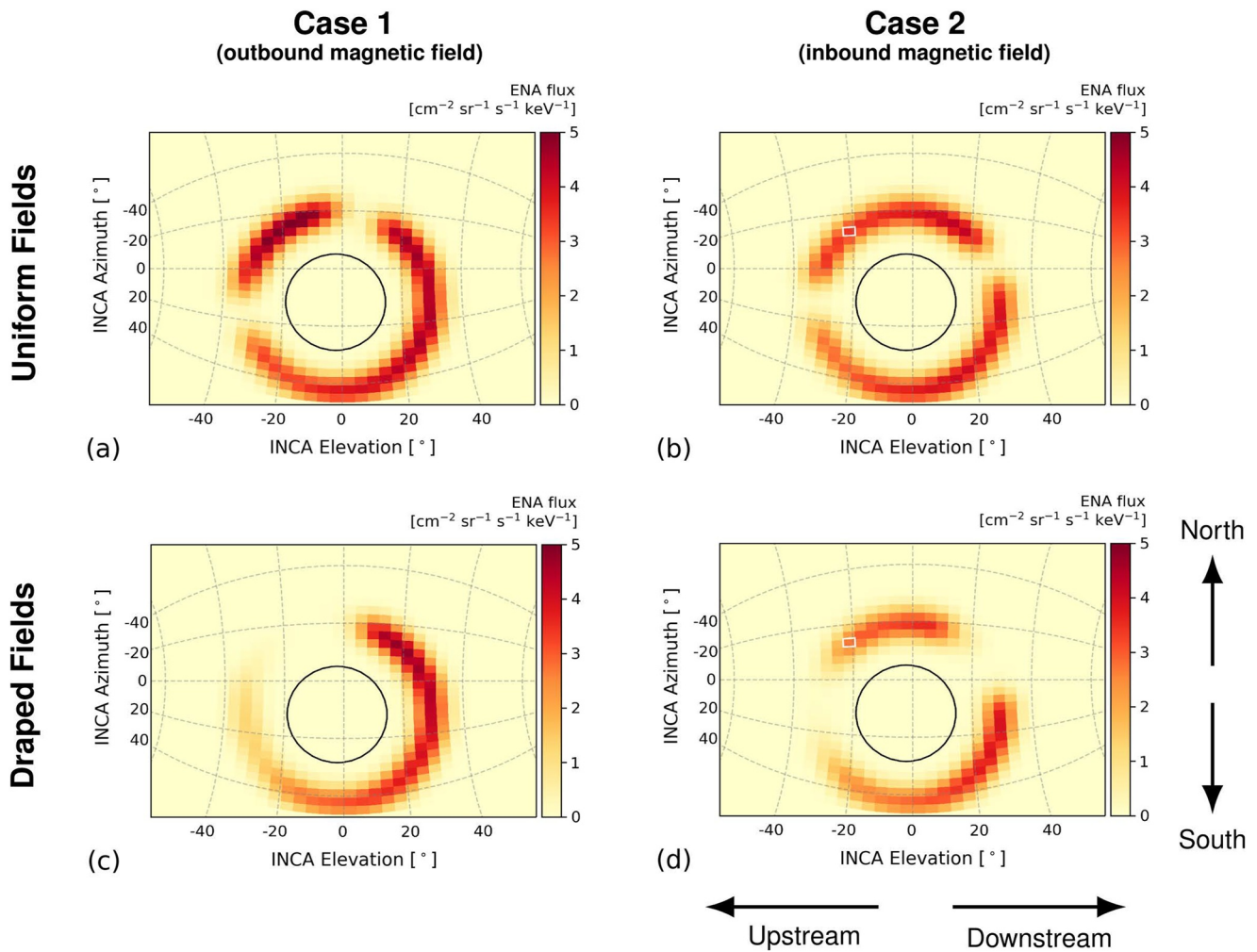


Figure 10. Synthetic ENA images for the TA flyby in uniform and draped fields, generated using the two different background magnetic field vectors from Table 1. The two images in the top row (panels (a, b)) were produced using uniform fields and the images in the bottom row (panels (c, d)) use the draped fields from AIKEF. The ambient magnetic field vectors for the left (panels (a, c)) and right (panels (b, d)) columns correspond to Cases 1 and 2 from Table 1, respectively. In all four model scenarios, the detector location and pointing are configured for TA as depicted in Figure 1. The images are formatted identically to those in Figure 7 and have been generated using the PSF parameters from Krimigis et al. (2004). The white squares in the right column indicate a pixel into which the sample parent ions shown in Figure 11 emit ENA flux. This is the same pixel for both panels (b, d). It is also the same pixel that is highlighted in Figure 7.

inbound leg of TA (Case 2 in Table 1). These backtraced ions are launched with the *same* position and velocity vectors on a detector LOS and possess *allowed* trajectories: the ENA flux emitted into the detector by the ions in columns 11(a) and (b) contributes to the pixel highlighted in white in Figures 10b and 10d, respectively. The launch conditions of these ions are also the same as those of the backtraced ions shown in Figures 8a and 8c. However, that model setup used the magnetospheric field $\vec{B}_{0,1}$ observed during the outbound leg of TA to calculate the draping pattern near Titan (Case 1 of Table 1). As can be seen in Figure 8, the ion's trajectory was allowed *only* in uniform fields, while in draped fields it was forbidden and did not contribute flux to the synthetic ENA image in Figures 7c and 10c. However, for Case 2 (Figure 11) the ion's trajectory is allowed in *both* uniform and draped fields.

When using the uniform field $\vec{B}_{0,1}$ from Case 1 (Figure 8a), the parent ion has a pitch angle of about 88° and enters the moon's interaction region from upstream before emitting ENA flux into the highlighted pixel in Figure 7b. However, when the fields are draped (Figure 7c), this proton gyrates repeatedly into the magnetic pile-up region upstream of Titan and is deflected away from the moon (Figure 8b). In the uniform field $\vec{B}_{0,2}$ from Case 2 (column 11(a)), an ion with the same launch conditions on the LOS has a somewhat steeper pitch angle of about 79° and (in forward-time) would originate north of Titan. In the draped fields from Case 2 (column 11(b)), this parent

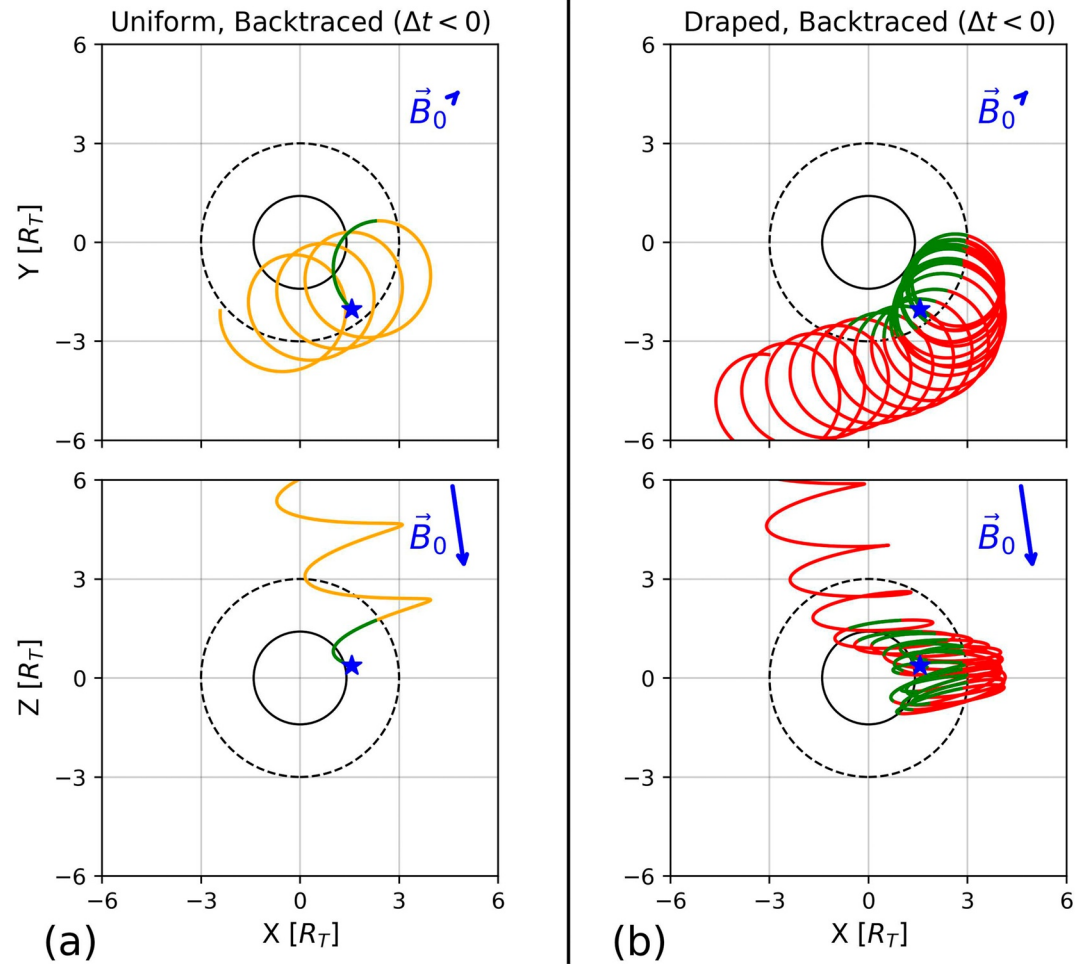


Figure 11. Two energetic parent proton trajectories traveling through Titan's electromagnetic environment. This setup includes the ambient magnetic field vector observed during the inbound leg of TA (Case 2 in Table 1). The individual panels are formatted similarly to those in Figure 8. Since the background magnetic field vector primarily points in $(-Z)$ direction, the blue arrows denoting the projection of \vec{B}_0 onto the $Z = 0$ plane in the top row are very small. Both columns show the (projected) trajectories of parent ions that have been traced backward in time until they reach unperturbed fields at distances greater than $10R_T$ from Titan. Both particles have identical launch conditions to the ion which was backtraced in Figure 8c: position $\vec{x}_0 = \{1.65, -2.09, 0.35\} R_T$ and velocity $\vec{v}_0 = \{1967, -1601, -522\}$ km/s, corresponding to an energy of $E = 35.0$ keV. In column (a) the ion is backtraced through uniform fields, and in column (b) it is backtraced through the draped fields produced by AIKEF for Case 2. For both field configurations, these ions have allowed trajectories. They both emit ENA flux along the same detector LOS into the pixel highlighted in white in Figures 10b and 10d.

ion entirely misses the upstream pile-up region and is able to access the moon's atmosphere. It emits ENA flux into the region of enhanced flux above Titan's northern hemisphere, thereby contributing to this feature's presence even in draped fields (Case 2, see panel 10(d)). In both uniform and draped fields, the trajectories in Case 2 (Figure 11) are different from those in Case 1 (Figure 8) due to the rotation of the ions' gyroplanes by the changed magnetospheric field vector.

The modeled ENA emission pattern is different between the two choices of \vec{B}_0 in both uniform and draped fields, but in the latter case (which is the more realistic scenario) the deviations are particularly drastic. Therefore, Figure 10 suggests that INCA observations of Titan's interaction region are strongly influenced by the omnipresent variabilities in the moon's magnetospheric environment, which take place on time scales comparable to those of a Titan flyby (e.g., Simon et al., 2010a, 2010b). While the observed ENA image shown in Figure 7a was taken during the inbound segment of TA (see Figure 1), it is much more similar to the synthetic ENA image produced using the background field vector $\vec{B}_{0,1}$ from the outbound segment (Figure 10). During about half of the 9-min integration period for the observed image, Cassini was located inside of Titan's interaction region where the

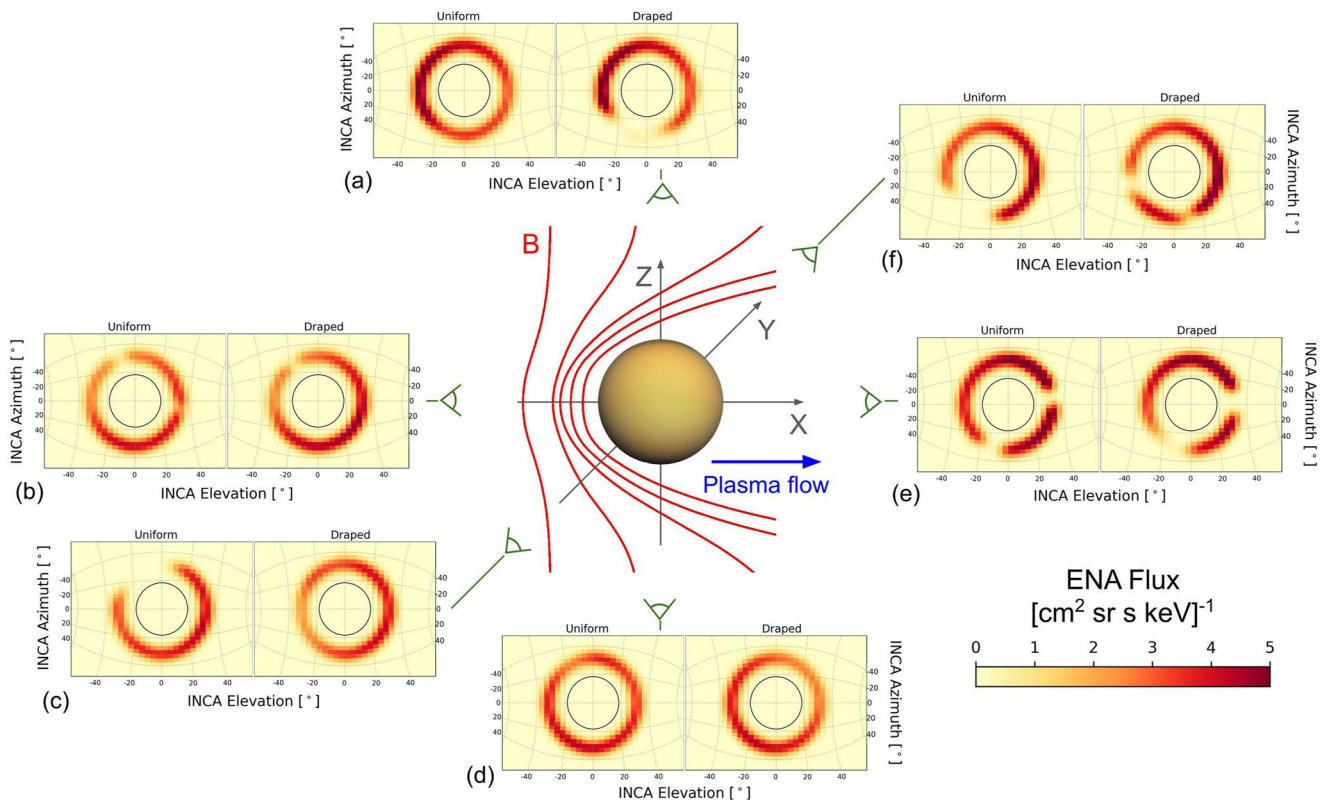


Figure 12. Synthetic ENA images in uniform and draped fields for six different detector locations, generated using the electromagnetic field conditions for TA (Case 1 in Table 1). The detector is placed at $2 R_T$ altitude at two different locations along each axis of the TIIS (colored gray): ($X = 0, Y = 0, Z = 3R_T$) for panel (a), ($X = -3R_T, Y = 0, Z = 0$) in panel (b), ($X = 0, Y = -3R_T, Z = 0$) in panel (c), ($X = 0, Y = 0, Z = -3 R_T$) for panel (d), ($X = 3R_T, Y = 0, Z = 0$) for panel (e), and ($X = 0, Y = 3R_T, Z = 0$) in panel (f). The boresight vector is always oriented toward the center of Titan. The six observation geometries are indicated by green observer symbols, which are connected to the corresponding pair of images by green lines. For each of the six detector locations and pointings, the left plot shows the synthetic ENA image in uniform fields and the right plot shows the modeled image in the draped fields obtained from AIKEF (see Figure 5). The plots are formatted in the same manner as Figures 7 and 10. Detector elevation lies on the horizontal axis and detector azimuth on the vertical axis; the 90° rotation of the detector during TA is maintained for consistency with the previously shown ENA images. To facilitate comparison, all images are displayed on the same color scale, depicted in the bottom right. The direction of the upstream plasma flow (+X) is shown in blue, and an illustration of the draped magnetic field lines near Titan is colored red.

field lines are draped and the actual background magnetic field is unknown (e.g., Backes et al., 2005; Neubauer et al., 2006). Thus, when making the assumption of a uniform, steady-state background field the “correct” ambient field vector associated with the ENA image from TA is ambiguous. The ENAs detected by INCA are largely produced non-locally (Tippens et al., 2022). Our results therefore suggest that the ambient field \vec{B}_0 at more remote locations in Titan's interaction region was already close to the outbound vector $\vec{B}_{0,1}$ (Case 1) when the TA image was taken. Alternatively, our modeled ENA images may indicate that the change in ambient field orientation from $\vec{B}_{0,2}$ (observed while inbound) to $\vec{B}_{0,1}$ (observed while outbound) did not progress gradually as Cassini traveled through Titan's interaction region. Rather, it may have occurred only shortly after the spacecraft had entered the draped fields.

3.4. Influence of the Detector Viewing Geometry

All of the synthetic ENA images we have presented in Sections 3.2 and 3.3 have been generated for the detector location and pointing during the TA flyby, as indicated by the orange dot in Figure 1. However, during its 126 close flybys Cassini captured ENA images of Titan's interaction region for numerous vantage points and detector orientations. As a first step to investigate the influence of the viewing geometry on the physics (e.g., the role of field line draping) captured by the ENA images, we have generated a set of synthetic ENA images for six different detector locations and pointings under the upstream plasma and magnetic field conditions during the outbound leg of TA (Case 1 in Table 1). The setup for this numerical experiment is illustrated in Figure 12: we place the detector at the top of Titan's atmosphere ($2 R_T$ altitude) along each axis of the TIIS: ($X = \pm 3R_T, Y = 0, Z = 0$),

($X = 0, Y = \pm 3R_T, Z = 0$), and ($X = 0, Y = 0, Z = \pm 3R_T$). At each of these six locations, we orient the detector exactly toward the center of Titan. Panels 12(a) and (d) show the images for the detector located directly above Titan's north/south poles ($X = 0, Y = 0, Z = \pm 3R_T$) and facing southward/northward along the ($\mp Z$) axis. Panels 12(b) and (e) represent the detector placed upstream/downstream of the moon ($X = \mp 3R_T, Y = 0, Z = 0$), with the boresight in the ($\pm X$) direction. The ENA images for the detector on the Saturn averted/facing side of Titan ($X = 0, Y = \mp 3R_T, Z = 0$), pointing directly toward/away from the planet along the ($\pm Y$) axis, are displayed in panels 12(c) and (f), respectively.

To facilitate comparison with the images examined thus far, we rotate the detector 90° clockwise around the boresight vector as was the case during TA. In panels 12(b), (c), (e), and (f) the axis measuring detector azimuth is parallel to the ($-Z$) axis of the TIIS, that is, azimuth grows with increasingly *negative* Z values. In panels 12(a) and (d), when the detector is located above Titan's north pole or below its south pole, respectively, the detector azimuth axis is parallel to the ($-Y$) axis (i.e., azimuth decreases toward Saturn). For each detector location and pointing, we have generated two synthetic ENA images: one using uniform fields ($\vec{B}_{0,1}$ and $\vec{E}_{0,1} = -\vec{u}_0 \times \vec{B}_{0,1}$) and one using draped fields. The images are again generated with the PSF parameters from Krimigis et al. (2004).

Panels 12(b), (d), and (e) show no qualitative changes and only minor quantitative differences between the ENA images in uniform and draped fields. These three sets of images correspond to the detector located upstream, south of Titan, and downstream, respectively. In the images for the upstream and downstream detector positions (panels 12(b) and (e)), there are narrow angular segments near Titan's disk where the ENA flux is approximately zero. When the detector is located below the south pole (panel 12(d)), the region of elevated ENA flux fully encircles the moon in both uniform and draped fields. When field line draping is considered for this detector location, the only difference from the ENA image in uniform fields is a small reduction in flux (by about 24%) above the upstream, Saturn-facing hemisphere (upper right quadrant of the images in panel 12(d)).

Clearly discernible effects of field line draping would be observable at the remaining three detector locations (panels 12(a), (c), and (f)). These are the images from detectors located north of Titan and in its Saturn-averted and Saturn-facing hemispheres, respectively. Note that the visibility of field line draping in the ENA images is different between detector positions north (panel 12(a)) and south (panel 12(d)) of Titan. Since the background field \vec{B}_0 is not aligned with the ($-Z$) axis, the moon's interaction region is not symmetric between the northern ($Z > 0$) and southern ($Z < 0$) half spaces. In panel 12(a), the region of elevated ENA flux completely encircles the moon in uniform fields, whereas in draped fields a segment of near-zero flux forms above the Saturn-averted hemisphere. While the detector's location and pointing are very different from those during TA, this effect of the field line draping (i.e., eliminating an angular segment of elevated ENA flux) is similar to what we found for the TA viewing geometry (see Figure 7).

However, when the detector is located in Titan's Saturn-averted or Saturn-facing hemispheres (panels 12(c) and (f)), the effect of the field line draping is reversed: in uniform fields the synthetic image contains an angular segment of near-zero ENA flux which is "filled in" when field draping is included. Thus, the location and pointing of the detector determine not only the visibility of the field draping in the ENA image, but also the qualitative influence of the draping. Depending on the location of the detector, a portion of the high-flux region may be depleted or a low-flux segment may be filled with ENAs when field line draping is considered. Alternatively, for certain vantage points and viewing directions, field line draping may not be discernible in the synthetic ENA images at all.

Of the six viewing geometries shown in Figure 12, the detector on the Saturn-averted side of Titan (panel 12(c)) is closest to Cassini's position during TA, which was used to generate the previously discussed synthetic ENA images (see Figures 7, 9, and 10). However, compared to the synthetic ENA images for the TA viewing geometry (Figure 7), the images produced for ($X = 0, Y = -3R_T, Z = 0$) display precisely the *opposite* effect of the field draping on the ENA morphology. Our results therefore suggest that it is more challenging than implied by earlier work (e.g., Wulms et al., 2010) to identify a characteristic ENA emission signature associated with field draping, especially when considering only a single flyby of Titan.

4. Summary and Concluding Remarks

In this study we present a novel method to support remote sensing of Titan's induced magnetosphere using ENA imaging. We trace energetic parent ions backward in time through the draped electromagnetic fields produced

by the AIKEF hybrid model (Müller et al., 2011) and generate synthetic ENA images using a realistic, point-like detector geometry with a limited field of view. Synthetic ENA images are generated by extending lines of sight from each pixel of the detector and launching energetic magnetospheric parent ions at several discrete energies along each LOS. These ions are then backtraced until their trajectories can be labeled *allowed* (i.e., the ions exit Titan's interaction region) or *forbidden* (i.e., they pass below the minimum passing distance). Our model determines the ENA flux emitted into each pixel of the detector by parent ions with allowed trajectories, and a synthetic ENA image is generated by summing the contributions of all such ions within the detector's 24–55 keV energy channel. The modeled images are then down-scaled to the resolution of observed INCA images and convolved with the instrument's point spread function (PSF). Our backtracing approach allows a sufficient number of ENAs to enter a point-like model detector to produce sharp ENA images. This was infeasible in preceding studies of ENA generation in draped fields, which initialized energetic ions outside of Titan's interaction region and traced them forward in time (Kabanovic et al., 2018; Tippens et al., 2022; Wulms et al., 2010).

We applied our model to analyze ENA observations made by INCA during Cassini's first close Titan flyby, TA on 26 October 2004. To determine how field line draping maps into the modeled ENA images, we produced synthetic images for both uniform magnetospheric fields and the draped fields produced by AIKEF. The model detector was positioned and oriented according to INCA's location and pointing during the inbound leg of TA. We took into account three different published sets of values for the width of the detector's PSF (Brandt et al., 2012; Dialynas et al., 2013; Krimigis et al., 2004).

The ambient magnetospheric conditions during TA were found to be highly variable: the background field vectors observed during the inbound and outbound segments of TA formed an angle of 33°, and their magnitudes differed by a factor of 1.2 (Neubauer et al., 2006). To assess the influence of ambient magnetospheric variability on the observed ENA images, we carried out model runs using either of these two vectors to represent the background magnetic field. We also sought to identify (hypothetical) viewing directions for INCA where, for the magnetospheric conditions during TA, the impact of field line draping on the observable ENA images would be clearly discernible. To this end, we produced additional synthetic ENA images for both uniform and draped fields with our model detector placed at six different, representative locations around Titan.

Our major findings are as follows:

1. By combining a realistic (i.e., point-like with a limited field of view) detector model with a backtracing method to determine the motion of energetic parent ions through the draped fields in Titan's interaction region, we can generate synthetic ENA images which reproduce both the intensity and the emission morphology observed during TA by Cassini's INCA instrument.
2. Utilizing such a realistic detector geometry is critical to constrain the role of field line draping in shaping the emission morphology of observed ENA images. In uniform fields, our synthetic ENA images show a segmented ring of elevated ENA flux surrounding Titan. When we include draping, an angular segment of this ring is eliminated from the synthetic image. A crescent of elevated flux remains above the moon's downstream hemisphere. The impact of field line draping revealed by our approach is different than suggested by previous modeling studies, which utilized an infinitely extended plane detector to capture all ENAs emitted in a certain direction. For example, Wulms et al. (2010) found that a crescent of elevated ENA flux is already formed in uniform fields, located above Titan's upstream hemisphere. These authors suggested that the inclusion of field line draping would mirror the crescent such that it wraps around the downstream hemisphere. Our results differ from those of Wulms et al. (2010) because their plane detector captures all ENAs emitted in one specific direction. However, the ENA trajectories observable by our model converge to a point-like location.
3. Our modeled ENA images must be convolved with the detector's PSF in order to produce quantitatively accurate synthetic images. However, within the range of PSF widths documented in the literature, this process only “smears out” the modeled images and does not change the overall morphology of the observable ENA flux pattern.
4. The omnipresent time variability of the ambient magnetospheric field vector \vec{B}_0 on timescales of the TA encounter (e.g., Simon et al., 2010b) does affect the morphology of ENA images and must be taken into account when interpreting INCA observations. When using the field vector measured in the outbound leg of TA, the inclusion of field line draping eliminates an angular segment of elevated ENA flux from the image (see item #2). When the ambient field vector from the inbound leg of TA is used, however, the observable emission morphology is qualitatively the same in both uniform and draped fields. Overall, our study highlights the potential of ENA images to remotely constrain the ambient magnetic field orientation at Titan, and hence the orientation of the steady-state DRAP coordinate system.

5. Our results for TA suggest that the draped magnetospheric fields, even at distant locations within Titan's interaction region, leave an imprint in the observed INCA images. This emphasizes the potential for remote sensing of the moon's plasma interaction using ENA imaging.
6. Our findings suggest that the visibility and qualitative influence of magnetic field line draping on the observed ENA emission morphology depend strongly on the detector's location and pointing. For the six representative detector locations we investigated under TA conditions (north, south, upstream, downstream, Saturn-facing, and Saturn-averted relative to Titan), we identified three distinct effects of draping on the ENA flux pattern observable by INCA. Depending on the viewing geometry, draping may add or remove features from the ENA image or have no discernible influence at all.

Overall, the INCA detector recorded ENA images during over 100 flybys of Titan. These observations cover all of the different Saturnian magnetospheric regimes to which the moon is exposed along its orbit (such as Saturn's magnetodisk current sheet or lobes). This vast, yet largely unexplored data set is ripe for future modeling work which would search for more robust, characteristic “fingerprints” of field line draping in INCA images that were taken under similar ambient magnetospheric conditions. In this way, modeling of the ENA emissions can produce a comprehensive picture of Titan's induced magnetosphere when exposed to the omnipresent time variabilities in the upstream conditions (Simon et al., 2013). For meaningful results, INCA images considered should have been taken sufficiently far away from Titan to capture ENAs that emanate from different parts of the interaction region, yet close enough to resolve features of interest with multiple pixels. Finally, our method is also suitable to generate synthetic ENA images for, for example, the upcoming JUICE flybys of Europa and Callisto. At both objects, field line draping has been found to strongly influence the global ENA emission morphology (Haynes et al., 2023), suggesting it may also be visible in ENA observations from JUICE. The work of Haynes et al. (2023) also revealed that the induced magnetic fields from these moons' subsurface oceans leave a subtle, yet clearly discernible signature in the ENA emission morphology.

Data Availability Statement

The data supporting this work can be obtained from Tippens et al. (2023).

Acknowledgments

Tyler Tippens and Sven Simon acknowledge financial support through NASA's Cassini Data Analysis Program 2022, Grant 80NSSC23K0215. The authors appreciate valuable input from Kostas Dialynas (Office of Space Research and Technology, Academy of Athens, Greece) on the model parameters for the Point Spread Function.

References

- Addison, P., Liuzzo, L., & Simon, S. (2022). Effect of the magnetospheric plasma interaction and solar illumination on ion sputtering of Europa's surface ice. *Journal of Geophysical Research: Space Physics*, 127(2), e2021JA030136. <https://doi.org/10.1029/2021JA030136>
- Addison, P., Liuzzo, L., & Simon, S. (2023). Surface-plasma interactions at Europa in draped magnetospheric fields: The contribution of energetic electrons to energy deposition and sputtering. *Journal of Geophysical Research: Space Physics*, 128(8), e2023JA031734. <https://doi.org/10.1029/2023JA031734>
- Amsif, A., Dandouras, J., & Roelof, E. C. (1997). Modelling the production and the imaging of energetic neutral atoms from Titan's exosphere. *Journal of Geophysical Research*, 102(A10), 22169–22181. <https://doi.org/10.1029/97ja01597>
- Arridge, C. S., Achilleos, N., & Guio, P. (2011a). Electric field variability and classifications of Titan's magnetoplasma environment. *Annales Geophysicae*, 29(7), 1253–1258. <https://doi.org/10.5194/angeo-29-1253-2011>
- Arridge, C. S., André, N., Bertucci, C. L., Garnier, P., Jackman, C. M., Németh, Z., et al. (2011b). Upstream of Saturn and Titan. *Space Science Reviews*, 162(1–4), 25–83. <https://doi.org/10.1007/s11214-011-9849-x>
- Arridge, C. S., Khurana, K. K., Russell, C. T., Southwood, D. J., Achilleos, N., Dougherty, M. K., et al. (2008). Warping of Saturn's magnetospheric and magnetotail current sheets. *Journal of Geophysical Research*, 113(A12), A08217. <https://doi.org/10.1029/2007JA012963>
- Backes, H., Neubauer, F. M., Dougherty, M. K., Achilleos, N., André, N., Arridge, C. S., et al. (2005). Titan's magnetic field signature during the first Cassini encounter. *Science*, 308(5724), 992–995. <https://doi.org/10.1126/science.1109763>
- Bagenal, F., & Delamere, P. A. (2011). Flow of mass and energy in the magnetospheres of Jupiter and Saturn. *Journal of Geophysical Research*, 116(A5), A05209. <https://doi.org/10.1029/2010JA016294>
- Bertucci, C., Hamilton, D. C., Kurth, W. S., Hospodarsky, G., Mitchell, D., Sergis, N., et al. (2015). Titan's interaction with the supersonic solar wind. *Geophysical Research Letters*, 42(2), 193–200. <https://doi.org/10.1002/2014GL062106>
- Bertucci, C., Neubauer, F. M., Szego, K., Wahlund, J.-E., Coates, A. J., Dougherty, M. K., et al. (2007). Structure of Titan's mid-range magnetic tail: Cassini magnetometer observations during the T9 flyby. *Geophysical Research Letters*, 34(24), L24S02. <https://doi.org/10.1029/2007GL030865>
- Bertucci, C., Sinclair, B., Achilleos, N., Hunt, P., Dougherty, M. K., & Arridge, C. S. (2009). The variability of Titan's magnetic environment. *Planetary and Space Science*, 57(14–15), 1813–1820. <https://doi.org/10.1016/j.pss.2009.02.009>
- Brandt, P., Dialynas, K., Dandouras, I., Mitchell, D., Garnier, P., & Krimigis, S. (2012). The distribution of Titan's high-altitude (out to ~50,000km) exosphere from energetic neutral atom (ENA) measurements by Cassini/INCA. *Planetary and Space Science*, 60(1), 107–114. <https://doi.org/10.1016/j.pss.2011.04.014>
- Chen, C., & Simon, S. (2020). A comprehensive study of Titan's magnetic pile-up region during the Cassini era. *Planetary and Space Science*, 191, 105037. <https://doi.org/10.1016/j.pss.2020.105037>
- Coates, A. J., Wahlund, J. E., Ågren, K., Edberg, N., Cui, J., Wellbrock, A., & Szego, K. (2011). Recent results from Titan's ionosphere. *Space Science Reviews*, 162(1–4), 85–111. <https://doi.org/10.1007/s11214-011-9826-4>

- Coates, A. J., Wellbrock, A., Lewis, G. R., Arridge, C. S., Crary, F. J., Young, D. T., et al. (2012). Cassini in Titan's tail: CAPS observations of plasma escape. *Journal of Geophysical Research*, *117*(A5), A05324. <https://doi.org/10.1029/2012JA017595>
- Cravens, T. E., Robertson, I. P., Clark, J., Wahlund, J.-E., Waite, J. H., Jr., Ledvina, S. A., et al. (2005). Titan's ionosphere: Model comparisons with Cassini TA data. *Geophysical Research Letters*, *32*(1–5), L12108. <https://doi.org/10.1029/2005gl023249>
- Cravens, T. E., Yelle, R. V., Wahlund, J. E., Shemansky, D. E., & Nagy, A. F. (2010). Composition and structure of the ionosphere and thermosphere. In R. H. Brown, J.-P. Lebreton, & J. H. Waite (Eds.), *Titan from Cassini-Huygens* (pp. 259–295). Springer Netherlands. https://doi.org/10.1007/978-1-4020-9215-2_11
- Cui, J., Yelle, R. V., Vuitton, V., Waite, J. H., Kasprzak, W. T., Gell, D. A., et al. (2009). Analysis of Titan's neutral upper atmosphere from Cassini ion neutral mass spectrometer measurements. *Icarus*, *200*(2), 581–615. <https://doi.org/10.1016/j.icarus.2008.12.005>
- Dandouras, J., & Amsif, A. (1999). Production and imaging of energetic neutral atoms from Titan's exosphere: A 3-D model. *Planetary and Space Science*, *47*(10–11), 1355–1369. [https://doi.org/10.1016/S0032-0633\(99\)00057-4](https://doi.org/10.1016/S0032-0633(99)00057-4)
- Dialynas, K., Brandt, P. C., Krimigis, S. M., Mitchell, D. G., Hamilton, D. C., Krupp, N., & Rymer, A. M. (2013). The extended Saturnian neutral cloud as revealed by global ENA simulations using Cassini/MIMI measurements. *Journal of Geophysical Research: Space Physics*, *118*(6), 3027–3041. <https://doi.org/10.1002/jgra.50295>
- Edberg, N. J. T., Andrews, D. J., Shebanits, O., Ågren, K., Wahlund, J.-E., Opgenoorth, H. J., et al. (2013). Extreme densities in Titan's ionosphere during the T85 magnetosheath encounter. *Geophysical Research Letters*, *40*(12), 2879–2883. <https://doi.org/10.1002/grl.50579>
- Fatemi, S., Holmström, M., & Futaana, Y. (2012). The effects of lunar surface plasma absorption and solar wind temperature anisotropies on the solar wind proton velocity space distributions in the low-altitude lunar plasma wake. *Journal of Geophysical Research*, *117*(A10), A10105. <https://doi.org/10.1029/2011JA017353>
- Feyerabend, M., Simon, S., Motschmann, U., & Liuzzo, L. (2015). Filamented ion tail structures at Titan: A hybrid simulation study. *Planetary and Space Science*, *117*, 362–376. <https://doi.org/10.1016/j.pss.2015.07.008>
- Feyerabend, M., Simon, S., Neubauer, F. M., Motschmann, U., Bertucci, C., Edberg, N. J. T., et al. (2016). Hybrid simulation of Titan's interaction with the supersonic solar wind during Cassini's T96 flyby. *Geophysical Research Letters*, *43*(1), 35–42. <https://doi.org/10.1002/2015GL066848>
- Galand, M., Coates, A. J., Cravens, T. E., & Wahlund, J.-E. (2014). Titan's ionosphere. In I. Müller-Wodarg, C. A. Griffith, E. Lellouch, & T. E. Cravens (Eds.), *Titan: Interior, surface, atmosphere, and space environment* (pp. 376–418). Cambridge University Press. <https://doi.org/10.1017/CBO9780511667398.014>
- Garnier, P., Dandouras, I., Toublanc, D., Roelof, E. C., Brandt, P. C., Mitchell, D. G., et al. (2010). Statistical analysis of the energetic ion and ENA data for the Titan environment. *Planetary and Space Science*, *58*(14–15), 1811–1822. <https://doi.org/10.1016/j.pss.2010.08.009>
- Garnier, P., Dandouras, I., Toublanc, D., Roelof, E. C., Brandt, P. C., Mitchell, D. G., et al. (2008). The lower exosphere of Titan: Energetic neutral atoms absorption and imaging. *Journal of Geophysical Research*, *113*(A12), A10216. <https://doi.org/10.1029/2008JA013029>
- Gurnett, D. A., Kurth, W. S., Kirchner, D. L., Hospodarsky, G. B., Averkamp, T. F., Zarka, P., et al. (2004). The Cassini radio and plasma wave investigation. *Space Science Reviews*, *114*(1), 395–463. <https://doi.org/10.1007/s11214-004-1434-0>
- Hartle, R. E., Sittler, E. C., Neubauer, F. M., Johnson, R. E., Smith, H. T., Crary, F., et al. (2006). Preliminary interpretation of Titan plasma interaction as observed by the Cassini plasma spectrometer: Comparisons with Voyager 1. *Geophysical Research Letters*, *33*(8), L08201. <https://doi.org/10.1029/2005GL024817>
- Haynes, C. M., Tippens, T., Addison, P., Liuzzo, L., Poppe, A. R., & Simon, S. (2023). Emission of energetic neutral atoms from the magnetosphere-atmosphere interactions at Callisto and Europa. *Journal of Geophysical Research: Space Physics*, *128*(10), e2023JA031931. <https://doi.org/10.1029/2023JA031931>
- Janev, R. K., & Reiter, D. (2002). Collision processes of CH_y and CH_y⁺ hydrocarbons with plasma electrons and protons. *Physics of Plasmas*, *9*(9), 4071–4081. <https://doi.org/10.1063/1.1500735>
- Kabanovic, S., Feyerabend, M., Simon, S., Meeks, Z., & Wulms, V. (2018). Influence of asymmetries in the magnetic draping pattern at Titan on the emission of energetic neutral atoms. *Planetary and Space Science*, *152*, 142–164. <https://doi.org/10.1016/j.pss.2017.12.017>
- Kane, M., Mitchell, D. G., Carbary, J. F., Dialynas, K., Hill, M. E., & Krimigis, S. M. (2020). Convection in the magnetosphere of Saturn during the Cassini mission derived from MIMI INCA and CHEMS measurements. *Journal of Geophysical Research: Space Physics*, *125*(2), e2019JA027534. <https://doi.org/10.1029/2019JA027534>
- Kollmann, P., Hill, M. E., McNutt, R. L., Brown, L. E., Allen, R. C., Clark, G., et al. (2019). Suprathermal ions in the outer heliosphere. *The Astrophysical Journal*, *876*(1), 46. <https://doi.org/10.3847/1538-4357/ab125f>
- Krimigis, S. M., Mitchell, D. G., Hamilton, D. C., Livi, S., Dandouras, J., Jaskulek, S., et al. (2004). Magnetosphere Imaging Instrument (MIMI) on the Cassini mission to Saturn/Titan. *Space Science Reviews*, *114*(1–4), 233–329. <https://doi.org/10.1007/s11214-004-1410-8>
- Lindsay, B. G., & Stebbings, R. F. (2005). Charge transfer cross sections for energetic neutral atom data analysis. *Journal of Geophysical Research*, *110*(A12), A12213. <https://doi.org/10.1029/2005JA011298>
- Lipatov, A., Sittler, E., Hartle, R., Cooper, J., & Simpson, D. (2014). Titan's plasma environment: 3D hybrid kinetic modeling of the TA flyby and comparison with CAPS-ELS and RPWS LP observations. *Planetary and Space Science*, *93*–94, 119–128. <https://doi.org/10.1016/j.pss.2014.02.012>
- Liuzzo, L., Poppe, A. R., Addison, P., Simon, S., Nénon, Q., & Paranicas, C. (2022). Energetic magnetospheric particle fluxes onto Callisto's atmosphere. *Journal of Geophysical Research: Space Physics*, *127*(11), e2022JA030915. <https://doi.org/10.1029/2022JA030915>
- Liuzzo, L., Simon, S., & Regoli, L. (2019). Energetic ion dynamics near Callisto. *Planetary and Space Science*, *166*, 23–53. <https://doi.org/10.1016/j.pss.2018.07.014>
- Ma, Y. J., Nagy, A. F., Cravens, T. E., Sokolov, I. V., Hansen, K. C., Wahlund, J.-E., et al. (2006). Comparisons between MHD model calculations and observations of Cassini flybys of Titan. *Journal of Geophysical Research*, *111*(A5), A05207. <https://doi.org/10.1029/2005JA011481>
- Mauk, B. H., Mitchell, D. G., Krimigis, S. M., Roelof, E. C., & Paranicas, C. P. (2003). Energetic neutral atoms from a trans-Europa gas torus at Jupiter. *Nature*, *421*(6926), 920–922. <https://doi.org/10.1038/nature01431>
- Mitchell, D. G., Brandt, P. C., Roelof, E. C., Dandouras, J., Krimigis, S. M., & Mauk, B. H. (2005). Energetic neutral atom emissions from Titan interaction with Saturn's magnetosphere. *Science*, *308*(5724), 989–992. <https://doi.org/10.1126/science.1109805>
- Mitchell, D. G., Cheng, A. F., Krimigis, S. M., Keath, E. P., Jaskulek, S. E., Mauk, B. H., & Drake, V. A. (1993). INCA: The ion neutral camera for energetic neutral atom imaging of the Saturnian magnetosphere. *Optical Engineering*, *32*(12), 3096–3101. <https://doi.org/10.1117/12.155609>
- Modolo, R., & Chanteur, G. M. (2008). A global hybrid model for Titan's interaction with the Kronian plasma: Application to the Cassini TA flyby. *Journal of Geophysical Research*, *113*(A12), A01317. <https://doi.org/10.1029/2007JA012453>
- Müller, J., Simon, S., Motschmann, U., Glassmeier, K. H., Saur, J., Schuele, J., & Pringle, G. J. (2010). Magnetic field fossilization and tail reconfiguration in Titan's plasma environment during a magnetopause passage: 3D adaptive hybrid code simulations. *Planetary and Space Science*, *58*(12), 1526–1546. <https://doi.org/10.1016/j.pss.2010.07.018>

- Müller, J., Simon, S., Motschmann, U., Schüle, J., Glassmeier, K.-H., & Pringle, G. J. (2011). A.I.K.E.F.: Adaptive hybrid model for space plasma simulations. *Computer Physics Communications*, 182(4), 946–966. <https://doi.org/10.1016/j.cpc.2010.12.033>
- Müller-Wodarg, I., Griffith, C., Lellouch, E., & Cravens, T. (Eds.). (2014). *Titan: Interior, Surface, atmosphere, and space environment*. Cambridge University Press. <https://doi.org/10.1017/CBO9780511667398>
- Németh, Z., Szego, K., Bebesi, Z., Erdős, G., Foldy, L., Rymer, A., et al. (2011). Ion distributions of different Kronian plasma regions. *Journal of Geophysical Research*, 116(A15), A09212. <https://doi.org/10.1029/2011JA016585>
- Ness, N. F., Acuna, M. H., Behannon, K. W., & Neubauer, F. M. (1982). The induced magnetosphere of Titan. *Journal of Geophysical Research*, 87(A3), 1369–1381. <https://doi.org/10.1029/JA087iA03p01369>
- Ness, N. F., Acuña, M. H., Lepping, R. P., Connerney, J. E. P., Behannon, K. W., Burlaga, L. F., & Neubauer, F. M. (1981). Magnetic field studies by Voyager 1: Preliminary results at Saturn. *Science*, 212(4491), 211–217. <https://doi.org/10.1126/science.212.4491.211>
- Neubauer, F. M., Backes, H., Dougherty, M. K., Wennmacher, A., Russell, C. T., Coates, A., et al. (2006). Titan's near magnetotail from magnetic field and plasma observations and modelling: Cassini flybys TA, TB and T3. *Journal of Geophysical Research*, 111(A10), A10220. <https://doi.org/10.1029/2006JA011676>
- Neubauer, F. M., Gurnett, D. A., Scudder, J. D., & Hartle, R. E. (1984). Titan's magnetospheric interaction. In T. Gehrels & M. S. Matthews (Eds.), *Saturn* (pp. 760–787). University of Arizona Press.
- Poppe, A. R., Fatemi, S., & Khurana, K. K. (2018). Thermal and energetic ion dynamics in Ganymede's magnetosphere. *Journal of Geophysical Research: Space Physics*, 123(6), 4614–4637. <https://doi.org/10.1029/2018JA025312>
- Regoli, L. H., Roussos, E., Dialynas, K., Luhmann, J. G., Sergis, N., Jia, X., et al. (2018). Statistical study of the energetic proton environment at Titan's orbit from the Cassini spacecraft. *Journal of Geophysical Research: Space Physics*, 123(6), 4820–4834. <https://doi.org/10.1029/2018JA025442>
- Regoli, L. H., Roussos, E., Feyerabend, M., Jones, G. H., Krupp, N., Coates, A. J., et al. (2016). Access of energetic particles to Titan's exobase: A study of Cassini's T9 flyby. *Planetary and Space Science*, 130, 40–53. <https://doi.org/10.1016/j.pss.2015.11.013>
- Richards, P. C., Fennelly, J. A., & Torr, D. G. (1994). EUVAC: A solar EUV flux model for aeronomic calculations. *Journal of Geophysical Research*, 99(A5), 8981–8992. <https://doi.org/10.1029/94ja00518>
- Russell, C. T., Wei, H. Y., Cowee, M. M., Neubauer, F. M., & Dougherty, M. K. (2016). Ion cyclotron waves at Titan. *Journal of Geophysical Research: Space Physics*, 121(3), 2095–2103. <https://doi.org/10.1002/2015JA022293>
- Rymer, A. M., Smith, H. T., Wellbrock, A., Coates, A. J., & Young, D. T. (2009). Discrete classification and electron energy spectra of Titan's varied magnetospheric environment. *Geophysical Research Letters*, 36(15), L15109. <https://doi.org/10.1029/2009GL039427>
- Simon, S., Boesswetter, A., Bagdonat, T., & Motschmann, U. (2007a). Physics of the ion composition boundary: A comparative 3D hybrid simulation study of Mars and Titan. *Annales Geophysicae*, 25(1), 99–115. <https://doi.org/10.5194/angeo-25-99-2007>
- Simon, S., Boesswetter, A., Bagdonat, T., Motschmann, U., & Glassmeier, K.-H. (2006). Plasma environment of Titan: A 3-d hybrid simulation study. *Annales Geophysicae*, 24(3), 1113–1135. <https://doi.org/10.5194/angeo-24-1113-2006>
- Simon, S., Boesswetter, A., Bagdonat, T., Motschmann, U., & Schuele, J. (2007b). Three-dimensional multispecies hybrid simulation of Titan's highly variable plasma environment. *Annales Geophysicae*, 25(1), 117–144. <https://doi.org/10.5194/angeo-25-117-2007>
- Simon, S., Kleindienst, G., Boesswetter, A., Bagdonat, T., Motschmann, U., Glassmeier, K.-H., et al. (2007c). Hybrid simulation of Titan's magnetic field signature during the Cassini T9 flyby. *Geophysical Research Letters*, 34, L24S08. <https://doi.org/10.1029/2007GL029967>
- Simon, S., & Motschmann, U. (2009). Titan's induced magnetosphere under non-ideal upstream conditions: 3D multi-species hybrid simulations. *Planetary and Space Science*, 57(14–15), 2001–2015. <https://doi.org/10.1016/j.pss.2009.08.010>
- Simon, S., Motschmann, U., & Glassmeier, K.-H. (2008). Influence of non-stationary electromagnetic field conditions on ion pick-up at Titan: 3-d multispecies hybrid simulations. *Annales Geophysicae*, 26(3), 599–617. <https://doi.org/10.5194/angeo-26-599-2008>
- Simon, S., Motschmann, U., Kleindienst, G., Glassmeier, K.-H., Bertucci, C., & Dougherty, M. K. (2008). Titan's magnetic field signature during the Cassini T34 flyby: Comparison between hybrid simulations and MAG data. *Geophysical Research Letters*, 35(4), L04107. <https://doi.org/10.1029/2007GL033056>
- Simon, S., Motschmann, U., Kleindienst, G., Saur, J., Bertucci, C., Dougherty, M., et al. (2009). Titan's plasma environment during a magnetosheath excursion: Real-time scenarios for Cassini's T32 flyby from a hybrid simulation. *Annales Geophysicae*, 27(2), 669–685. <https://doi.org/10.5194/angeo-27-669-2009>
- Simon, S., Roussos, E., & Paty, C. S. (2015). The interaction between Saturn's moons and their plasma environments. *Physics Reports*, 602, 1–65. <https://doi.org/10.1016/j.physrep.2015.09.005>
- Simon, S., van Treeck, S. C., Wennmacher, A., Saur, J., Neubauer, F. M., Bertucci, C. L., & Dougherty, M. K. (2013). Structure of Titan's induced magnetosphere under varying background magnetic field conditions: Survey of Cassini magnetometer data from flybys TA-T85. *Journal of Geophysical Research: Space Physics*, 118(4), 1679–1699. <https://doi.org/10.1002/jgra.50096>
- Simon, S., Wennmacher, A., Neubauer, F., Bertucci, C., Kriegel, H., Saur, J., & Dougherty, M. (2010a). Dynamics of Saturn's magnetodisk near Titan's orbit: Comparison of Cassini magnetometer observations from real and virtual Titan flybys. *Planetary and Space Science*, 58(12), 1625–1635. <https://doi.org/10.1016/j.pss.2010.08.006>
- Simon, S., Wennmacher, A., Neubauer, F., Bertucci, C., Kriegel, H., Saur, J., et al. (2010b). Titan's highly dynamic magnetic environment: A systematic survey of Cassini magnetometer observations from flybys TA–T62. *Planetary and Space Science*, 58(10), 1230–1251. <https://doi.org/10.1016/j.pss.2010.04.021>
- Snowden, D., Winglee, R., Bertucci, C., & Dougherty, M. (2007). Three-dimensional multifluid simulation of the plasma interaction at Titan. *Journal of Geophysical Research*, 112(A11), A12221. <https://doi.org/10.1029/2007JA012393>
- Szego, K., Bebesi, Z., Erdos, G., Foldy, L., Crary, F., McComas, D. J., et al. (2005). The global plasma environment of Titan as observed by Cassini Plasma Spectrometer during the first two close encounters with Titan. *Geophysical Research Letters*, 32(20), L20S05. <https://doi.org/10.1029/2005gl022646>
- Teolis, B. D., Niemann, H. B., Waite, J. H., Gell, D. A., Perryman, R. S., Kasprzak, W. T., et al. (2015). A revised sensitivity model for Cassini INMS: Results at Titan. *Space Science Reviews*, 190(1), 47–84. <https://doi.org/10.1007/s11214-014-0133-8>
- Thomsen, M. F., Reisenfeld, D. B., Delapp, D. M., Tokar, R. L., Young, D. T., Crary, F. J., et al. (2010). Survey of ion plasma parameters in Saturn's magnetosphere. *Journal of Geophysical Research*, 115(A10), A10220. <https://doi.org/10.1029/2010JA015267>
- Tippens, T., Liuzzo, L., & Simon, S. (2022). Influence of Titan's variable electromagnetic environment on the global distribution of energetic neutral atoms. *Journal of Geophysical Research: Space Physics*, 127(10), e2022JA030722. <https://doi.org/10.1029/2022JA030722>
- Tippens, T., Roussos, E., Simon, S., & Liuzzo, L. (2023). Data for “A novel backtracking model to study the emission of energetic neutral atoms at Titan” by Tippens et al., 2023 [Dataset]. Zenodo. <https://doi.org/10.5281/zenodo.8322674>
- Wahlund, J.-E., Boström, R., Gustafsson, G., Gurnett, D. A., Kurth, W. S., Pedersen, A., et al. (2005). Cassini measurements of cold plasma in the ionosphere of Titan. *Science*, 308(5724), 986–989. <https://doi.org/10.1126/science.1109807>

- Waite, J. H., Niemann, H., Yelle, R. V., Kasprzak, W. T., Cravens, T. E., Luhmann, J. G., et al. (2005). Ion neutral mass spectrometer results from the first flyby of Titan. *Science*, *308*(5724), 982–986. <https://doi.org/10.1126/science.1110652>
- Westlake, J. H., Bell, J. M., Waite, J. H., Jr., Johnson, R. E., Luhmann, J. G., Mandt, K. E., et al. (2011). Titan's thermospheric response to various plasma environments. *Journal of Geophysical Research*, *116*(A3), A03318. <https://doi.org/10.1029/2010JA016251>
- Wulms, V., Saur, J., Strobel, D. F., Simon, S., & Mitchell, D. G. (2010). Energetic neutral atoms from Titan: Particle simulations in draped magnetic and electric fields. *Journal of Geophysical Research*, *115*(A14), A06310. <https://doi.org/10.1029/2009JA014893>
- Young, D. T., Berthelier, J. J., Blanc, M., Burch, J. L., Coates, A. J., Goldstein, R., et al. (2004). Cassini plasma spectrometer investigation. *Space Science Reviews*, *114*(1–4), 1–112. <https://doi.org/10.1007/s11214-004-1406-4>